Optimal sparse networks for synchronization of semiconductor lasers

LI-LI YE,[1] NATHAN VIGNE,[2] FAN-YI LIN,[2,3] HUI CAO,[2,5] AND YING-CHENG LAI[1,4,*]

[1]*School of Electrical, Computer and Energy Engineering, Arizona State University, Tempe, Arizona 85287, USA*
[2]*Department of Applied Physics, Yale University, New Haven, Connecticut 06520, USA*
[3]*Institute of Photonics Technologies, Department of Electrical Engineering, National Tsing Hua University, Hsinchu 30013, Taiwan*
[4]*Department of Physics, Arizona State University, Tempe, Arizona 85287, USA*
[5]*hui.cao@yale.edu*
[*]*Ying-Cheng.Lai@asu.edu*

Abstract: The inevitable random frequency differences among semiconductor lasers present an obstacle to achieving their collective coherence, but previous worked showed that fully (all-to-all) coupled networks can still be synchronized even in the weakly coupling regime. An outstanding question is whether sparsely coupled network structures exist that lead to strong synchronization. This paper gives an affirmative answer: optimal sparse coupling configurations can be found which enables near-complete synchronization. Quite surprisingly, with respect to synchronization, certain sparse networks can outperform fully coupled networks, when the weights of coupling are placed dominantly on the laser pairs with large frequency differences. The counterintuitive phenomenon can be explained by a thermodynamic potential theory that maps the time-delay-induced phase dynamics to an energy landscape. These findings suggest a scalable and cost-effective approach to achieving robust, steady-state synchronization of semiconductor lasers in the presence of disorder and noise.

1. Introduction

Synchronization, the spontaneous alignment of phases and frequencies among interacting oscillators, is a fundamental phenomenon underlying the collective behavior of diverse physical, biological, and engineered systems [1–7]. An important application is laser synchronization, i.e., frequency and phase locking of coupled lasers, to generate an intense coherent beam [8–13]. Over the years, various coupling schemes have been developed for lasers, e.g., nearest-neighbor coupling, long-range coupling, global or all-to-all coupling [14–24]. More recently, laser arrays with non-Hermitian coupling [25–29] or supersymmetry [30, 31], as well as topological insulator laser arrays [32, 33], have been realized. A major obstacle to synchronizing a large number of lasers is intrinsic frequency detuning among the lasers. While the all-to-all coupling structure is most efficient for laser synchronization, it is hard to implement for a large array. In this regard, semiconductor lasers are of particular interest as their compact size and high efficiency enable a large-scale integration. How to achieve synchronization of semiconductor lasers with minimum coupling cost is the question to be addressed here.

For complex networks of nonlinear oscillators, the network topology can be optimized for global synchronization [5–7, 34–46]. For non-identical Kuramoto oscillators, the synchrony-optimized coupling architectures were identified and the stability was analyzed [47–55]. Coordinated removal of network links was shown to stabilize synchronization by making the completely synchronized state the sole attractor, leading to sparsity-driven synchronization [56]. These findings suggest the possibility of optimizing the connectivity of a sparse laser network for global synchronization, but the question remains outstanding of whether such optimal sparse network structure exists. Experimentally, selective connectivity is feasible by programmable

laser coupling with a spatial light modulator (SLM) [57].

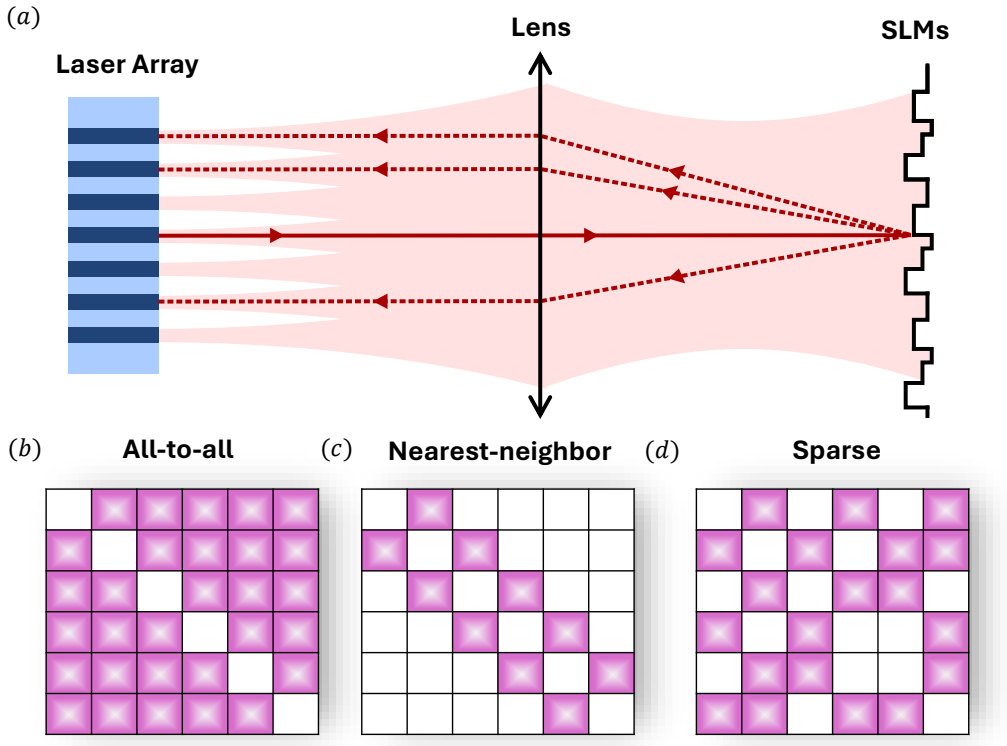

Fig. 1. Schematic diagram of laser coupling architectures. (a) Programmable laser coupling via SLMs. (b–d) Candidate coupling structures for synchronization under frequency disorder: long-range, short-range, and selectively sparse configurations.

This work provides an affirmative answer to this question. In particular, we investigate the global synchronization in sparsely coupled networks of semiconductor lasers with random frequency detuning. Previous works revealed that the linewidth enhancement factor, which couples the field amplitude fluctuations to phase, can destabilize the phase synchronization [58–60]. A recent theoretical study suggested that introducing disorder to the time-delay of laser coupling to counter-balance the frequency disorder can enhance synchronization [11]. Our focus is on finding the optimal sparse coupling configuration for frequency and phase locking. We begin by solving the Lang-Kobayashi equations systematically for semiconductor lasers with time-delayed coupling [61] and calculating the order parameter characterizing synchronization. We then exploit an island-based genetic algorithm to identify the optimal sparsity of laser coupling that maximizes the order parameter, which decreases as the number of lasers increases. This has led to some optimal sparse networks with near-perfect in-phase synchronization. We find that the optimal sparse networks share a common feature: the laser pairs with larger frequency difference are more likely to connect. For example, the lasers with larger frequency detuning from the mean frequency have more connections, preferably to the lasers with opposite frequency detuning. Surprisingly, the optimal sparse networks outperform the homogeneous all-to-all coupled networks in synchronization, sustaining robust frequency and phase locking even with substantial variations in natural lasing frequencies. We develop a thermodynamic potential theory to explain these phenomena, wherein the delayed phase dynamics are recast as a gradient flow on a potential landscape with the steady states corresponding to the local minima. The

theory predicts that the optimal sparsity is inversely proportional to the number of lasers, which agrees with the numerical results. Our findings suggest the efficacy of strategically designed sparse topologies in mitigating intrinsic disorders through selective connectivity, pointing toward a resource-efficient and experimentally feasible route for large-scale laser synchronization.

2. Results

2.1. Model description and parameter setting

Figure 1(a) illustrates a laser array coupled externally through an SLM. The array is at the front focal plane of an optical lens and the SLM is placed at the back focal plane. The lasers at different transverse locations are coupled via the gratings of corresponding periods on the SLM. The coupling is delayed by the round-trip time τ between the SLM and the laser array. Light reflection from the SLM forms an external cavity with resonant frequencies separated by $1/\tau$. In the absence of the SLM, each laser operates in a single longitudinal and transverse mode. Their intrinsic lasing frequencies deviate randomly due to the inevitable heterogeneity generated, e.g., during the manufacturing process.

A network of externally coupled semiconductor lasers with gain saturation and amplitude-phase coupling is mathematically described by the Lang-Kobayashi (LK) equations [11, 61]:

$$\frac{dE_i(t)}{dt} = \frac{1+i\alpha}{2}\left(g\frac{N_i(t)-N_0}{1+s|E_i(t)|^2}-\gamma\right)E_i(t) + i\Delta_i E_i(t) + e^{-i\omega_0\tau}\sum_{j=1}^{M}K_{ij}E_j(t-\tau) + F_{E_i}, \tag{1}$$

$$\frac{dN_i(t)}{dt} = J_0 - \gamma_n N_i(t) - g\frac{N_i(t)-N_0}{1+s|E_i(t)|^2}|E_i(t)|^2 + F_{N_i}, \tag{2}$$

where $E_i(t)$ is the complex electric field of the ith laser and $N_i(t)$ is its carrier number at the pump rate $J_0 = 4J_{\text{th}}$ with $J_{\text{th}} = \gamma_n(N_0 + \gamma/g)$. Here, γ_n, N_0, γ, and g represent the carrier decay rate, the carrier number at transparency threshold, the cavity loss rate, and the differential gain coefficient, respectively. The typical values of these parameters are $\gamma_n = 0.5\,\text{ns}^{-1}$, $N_0 = 1.5\times10^8$, $\gamma = 500\,\text{ns}^{-1}$, and $g = 1.5\times10^{-5}\,\text{ns}^{-1}$. The linewidth enhancement factor that characterizes the amplitude-phase coupling is $\alpha = 5$, and the gain saturation is described by $s = 2\times10^{-7}$. The external time delay is set to $\tau = 3\,\text{ns}$. The natural frequency detuning of the ith laser is $\Delta_i = \sigma_\Delta\,\mathcal{N}(0,1)$, where σ_Δ is the magnitude of frequency detuning and $\mathcal{N}(0,1)$ is a Gaussian random variable with zero mean and unit variance. The reference ω_0 of the natural angular frequencies is chosen to satisfy $\omega_0\tau = 2N\pi$, where N is an integer and selected to be closest to the mean of all laser frequencies. For convenience, we number the lasers by their frequency detuning from low to high: $\Delta_1 \le \Delta_2 \le \ldots \le \Delta_M$. (This numbering scheme is not related to the spatial distance between the lasers.) Spontaneous emission is introduced to the LK equations as noise for the electric field, $\langle F_{E_i}(t), F^*_{E_j}(t')\rangle = R_{sp}\delta_{ij}\delta(t-t')$, where R_{sp} is the spontaneous emission rate. Stochastic fluctuations in the carrier dynamics are given by $\langle F_{N_i}(t), F_{N_j}(t')\rangle = \gamma_n N_i(t)\delta_{ij}\delta(t-t')$.

With external coupling, the electric field of the ith laser is $E_i(t) = r_i(t)e^{i\Omega_i(t)}$, where $r_i(t)$ is the time-varying amplitude and Ω_i is the phase. The short-term frequency $\tilde{\Delta}_i$ is extracted from linear fitting $\Omega_i(t) = \tilde{\Delta}_i\,t + \varphi_i(t)$ over a short time window around t, and $\varphi_i(t)$ is phase fluctuation. Complete synchronization, encompassing field amplitude, frequency, and phase, is quantified by the order parameter $\langle S\rangle = \langle|\sum_{i=1}^{M}E_i(t)|^2/[M\sum_{i=1}^{M}|E_i(t)|^2]\rangle \in [0,1]$, where $\langle S\rangle = 1$ corresponds to all lasers having identical field amplitude, frequency and phase. Note that typical phase locking requires only the relative phase between lasers to be constant. A zero relative phase corresponds to in-phase locking. Note that, in-phase-locked lasers will produce a

single lobe of highest intensity in the far field via constructive interference, which is often needed for applications.

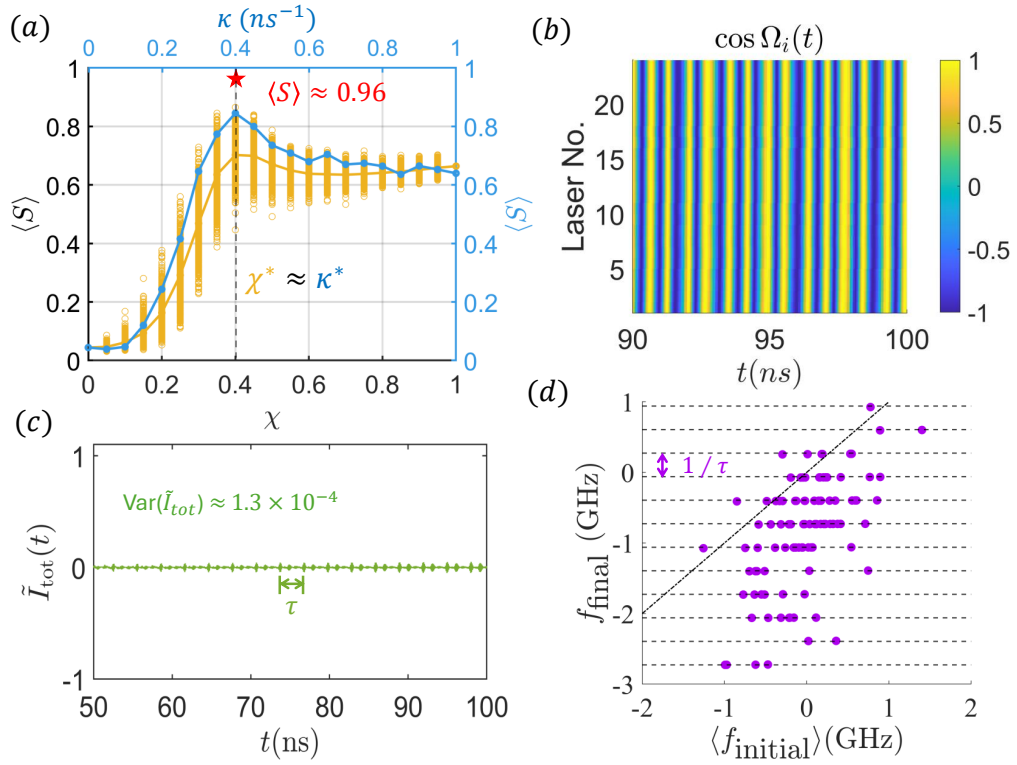

Fig. 2. Optimal synchronization state and coupling configuration for $M = 24$ lasers. (a) Connectivity resonance in sparse networks with frequency disorders: shown are $\langle S \rangle$ values from 1000 random sparse networks for different χ values, with the orange curve being the average. The red star marks the high value $\langle S \rangle = 0.96$ in an optimized sparse network for $\chi^* = 0.4$ found by a genetic algorithm. The blue curve represents the benchmark corresponding to the homogeneous all-to-all coupling, defined by $K_{ij} = \kappa(1 - \delta_{ij})$. (b) Spatiotemporal evolution of the phase function $\cos \Omega_i(t)$ of the laser field and (c) time series of the normalized total field intensity $\tilde{I}_{\text{tot}}$ for the optimal sparse network. (d) Scatter plot of the final frequencies f_{final} of the synchronized lasers versus their initial mean $\langle f_{\text{initial}} \rangle$ for 100 frequency-disorder realizations, corresponding to 100 data points, respectively. The final frequencies are quantized in intervals of N/τ. Points below the dashed line indicate that the final frequency is statistically lower than the initial mean frequency. Parameter values are: pump rate $J_0 = 4\gamma_n(N_0 + \gamma/g) \approx 3.67 \times 10^8$ ns^{-1} and $\sigma_\Delta = 14$ rad/ns.

2.2. *Optimal sparse laser networks with stronger synchronization than all-to-all coupled networks*

We begin with random sparse networks of lasers. Staring from an all-to-all coupled network of lasers with identical coupling coefficient, we randomly remove some links, leading to a sparsely coupled network, as illustrated in Fig. 1(d), where the coupling coefficients are $K_{ij} = 0$ or 1 ns^{-1} and self-feedback is ignored ($K_{ii} = 0$. The network connectivity is defined as the ratio between

the total number of links and the maximally possible number of links:

$$\chi \equiv \sum_{i,j} K_{ij}/[M(M-1)\kappa^f] \tag{3}$$

with coefficient $\kappa^f = 1\ \mathrm{ns}^{-1}$ to explicitly include the physical unit ns^{-1}. We simulate the dynamics of the sparse network for $t \in [0, 100]$ ns and calculate the order parameter $\langle S\rangle$ for $t \in [50, 100]$ ns to avoid transient dynamics. We repeat the calculation for different random networks with the same connectivity χ. The orange symbols in Fig. 2(a) represent $\langle S\rangle$ values for individual networks and the orange curve is the average $\langle S\rangle$ over all random configurations of the same χ. As χ increases continuously from zero to one, $\langle S\rangle$ first increases rapidly and then decrease gradually. The maximum value of $\langle S\rangle$ gives the optimum connectivity χ^* for synchronization resonance in terms of connectivity, which we refer to as connectivity resonance.

Synchronization resonance also occurs as a function of the coupling strength in homogeneous all-to-all networks [60]. In particular, coupling resonance is robust to the network structure, including inhomogeneous networks, as shown in SI Sec. 1. For comparison, we simulate the homogeneous networks with all-to-all coupling $K_{ij} = \kappa$ for $i \neq j$ but with no self-feedback. The lasers have the same frequency disorder as for the sparse case. The blue curve in Fig. 2(a) shows that the order parameter $\langle S\rangle$ first increases with the coupling strength κ and then decreases slightly, leading to an optimum κ^*. To compare with the randomly connected sparse networks, we define the coupling cost as the sum of all coupling coefficients. With the same coupling cost, $\langle S\rangle$ for all-to-all coupling is slightly higher than the average $\langle S\rangle$ of random sparse networks. However, a few random sparse network configurations have larger $\langle S\rangle$ than the maximum value achieved by the all-to-all network. Furthermore, connectivity resonance is consistently observed across different frequency disorders and initial seeds, as detailed in SI Sec. 2.

The result in Fig. 2(a) suggests that some sparse network may be optimized to outperform homogeneous all-to-all coupled networks in terms of synchronization. To find such optimal sparse networks, we fix the network connectivity at χ^*, set the coupling coefficient as that for the random networks in Fig. 2(a), and use an island-based genetic algorithm to search for the coupling configuration that gives the highest possible value of $\langle S\rangle$. For $M = 24$ lasers, the maximum $\langle S\rangle$ value is about 0.96 for $\chi^* = 0.4$, as indicated by the red star in Fig. 2(a). Note that this value is significantly higher than $\langle S\rangle \approx 0.84$ - the best that can be achieved for homogeneous all-to-all coupled networks. The near-unity $\langle S\rangle$ value indicates almost perfect synchronization of all lasers in terms of frequency, phase, and amplitude, despite their original frequency differences. Figure 2(b) shows $\cos[\Omega_i(t)]$ versus time t for each laser, which confirms frequency and in-phase locking of all lasers. In fact, the synchronized lasers reach a continuous-wave steady state, where the total intensity $I_{\mathrm{tot}}(t) = |\sum_i E_i(t)|^2$ exhibits small and negligible fluctuations in time, which can be quantified by the normalized total intensity: $\tilde{I}_{\mathrm{tot}}(t) \equiv (I_{\mathrm{tot}}(t) - \langle I_{\mathrm{tot}}\rangle)/\langle I_{\mathrm{tot}}\rangle$, as shown in Fig. 2(c). The corresponding mean square of relative intensity noise (RIN) is given by $\mathrm{Var}(\tilde{I}_{\mathrm{tot}}(t)) \approx 1.3 \times 10^{-4}$ for $t \in [50, 100]$ ns. The network optimization process is repeated with 100 statistically independent realizations of the frequency disorder, yielding $\langle S\rangle = 0.97 \pm 0.009$. The final locked frequency is close to, but slightly lower than, the mean of the original frequencies of all lasers, as a result of the positive α factor (see Sec. 3 3.4 for details). As shown in Fig. 2(d), the final frequencies of 100 synchronized networks, each optimized for its corresponding frequency disorder, are the discrete frequencies of external cavity resonances spaced by $1/\tau$.

2.3. Final frequency dynamics and scaling of connectivity resonance

In this section, we present the final frequencies of all lasers as a function of connectivity. At each χ, the final frequencies are obtained from the coupling configuration that yields the maximum $\langle S\rangle$ in random sampling. Figures 3(a) and 3(b) illustrate that, in the initial stage of connectivity

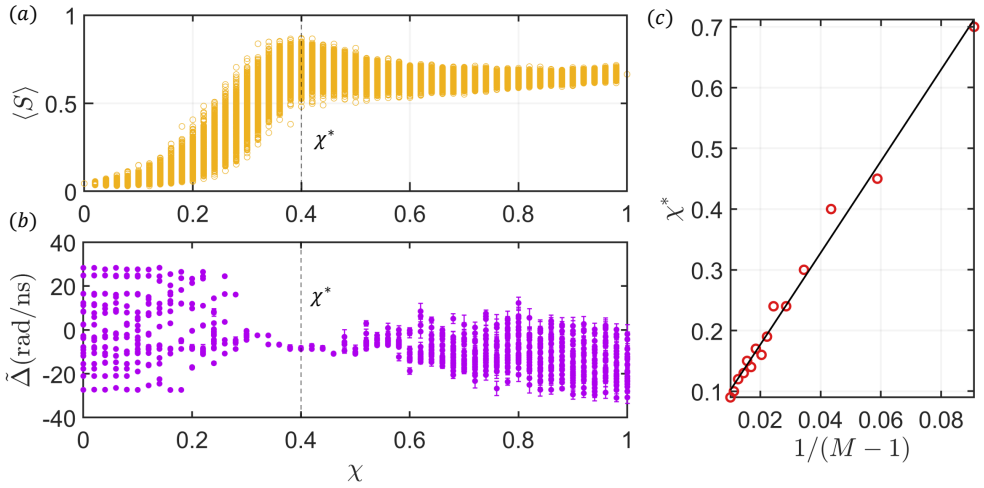

Fig. 3. Scaling of connectivity resonance. (a) For a fixed frequency disorder with random seed `rng(1)` (as in Fig. 2(a)), 1000 coupling configurations are randomly generated at each connectivity χ, and the corresponding $\langle S\rangle$ values are shown. (b) For each χ in (a), the configuration yielding the highest $\langle S\rangle$ is used to compute the final frequencies of all lasers. These frequencies are linearly fitted within moving windows of size τ with a step size of 0.1τ, and the error bars indicate the resulting standard deviations. (c) Using the same random seed `rng(1)`, the scaling behavior of the optimal connectivity χ^* is examined across different laser numbers $M = [12, 18, 24, 30, 36, 42, 46, 50, 55, 60, 65, 70, 80, 90, 100]$.

resonance, the final frequencies are well separated. As χ approaches the vicinity of χ^*, they collapse toward a single value. Beyond this optimal point χ^*, further increasing χ leads to strong fluctuations in the final frequencies, indicating that the system has moved away from a steady state and entered a chaotic regime. This behavior highlights that the optimal χ occurs just before the onset of chaos, with the chaotic dynamics being responsible for the subsequent decrease of $\langle S\rangle$ and the emergence of connectivity resonance. This dynamical explanation parallels our previous results on coupling resonance in homogeneous all-to-all coupled networks [60].

Furthermore, numerical evidence shows that the optimal connectivity scales with the number of lasers as $\chi^* \propto 1/(M-1)$. The slight deviation arises from the statistical deviation of the frequency disorder. The theoretical explanation of this scaling law is provided in Sec. 3 3.4.

2.4. Physical characteristics of optimal sparse networks

In homogeneous all-to-all coupled networks, more links are connected for smaller frequency differences in the histogram of the percentage of links versus the natural frequency difference $\Delta_i - \Delta_j$, as shown in Fig. 4(a). The reason is that Gaussian-distributed frequencies are more likely to be close to each other. In contrast, for optimal sparse networks, most links with nearby frequencies are removed, as shown in Fig. 4(b). Figure 4(c) shows the average of optimized coupling matrix elements over 100 frequency disorders, which confirms that the lasers with larger frequency difference have stronger coupling. This can be further seen from Fig. 4(d), the number of links for each laser, where the lasers with largest frequency offset from the mean have the highest number of links, so they are effectively "hub" lasers. Note that the concept of hub naturally arises in star networks [62–67], where a hub mediates the coupling among the lasers and serves as the "bridge" for synchrony. In our optimized sparse network, the hub lasers have the largest frequency detuning and are most difficult to be locked in frequency. As a result, more

links of such lasers to other lasers, especially those with opposite frequency detuning, are needed to pull the hub laser frequencies to the mean.

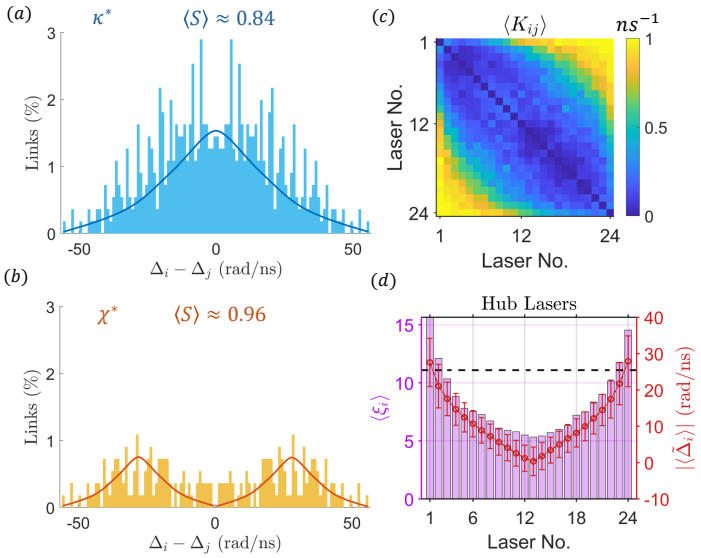

Fig. 4. Emergence of hub structure in the optimal sparse laser network. (a) Histogram of the percentage of coupled links as a function of the frequency differences $\Delta_i - \Delta_j$ $(i, j = 1, \ldots, M)$ for optimal coupling $\kappa = \kappa^*$ in homogeneous all-to-all coupled networks. The continuous curve illustrates the shape of the distribution. (b) Same legend as in (a) but for the optimal sparse laser networks found by the genetic algorithm. (c) Heat maps of the mean $\langle K_{ij}\rangle$ of the coupling matrix elements K_{ij} for the optimal sparse networks, averaged over 100 frequency disorder realizations. (d) Histogram of the average number of connections per laser, defined as $\langle \xi_i \rangle = \sum_j \langle K_{ij}/\kappa^f \rangle$ and calculated from the matrix elements in (c), for the optimal sparse networks. The horizontal dashed line indicates the baseline given by the mean value, $\mu_{\langle \xi \rangle} = \sum_i \langle \xi_i \rangle / M$, plus one standard deviation, $\sigma_{\langle \xi \rangle}$. Hub lasers are defined as those with $\langle \xi_i \rangle$ exceeding this baseline. Also shown on the right-hand side is the absolute value of the initial frequency detuning per laser averaged over 100 frequency disorder realizations, with standard deviations indicated by the error bars.

3. Heuristic and physical understanding of optimal synchronization in sparse laser networks

In this section, we provide a physical understanding of three key questions: (1) Why can a sparse network, with the same coupling cost as a homogeneous all-to-all network, outperform the latter in synchronization and even achieve near-complete coherence? (2) Why does an optimal connectivity scaling law emerge in connectivity resonance? (3) Why does the optimal sparse network develop an emergent hub structure?

3.1. Coupled linear oscillators

We first articulate a qualitative understanding of the optimal sparse network topology with a simple model of coupled linear oscillators (see Sec. 3 in SI). In particular, ignoring gain saturation, α factor and time-delay of the coupling, we calculate the eigenstates (supermodes) of the coupled lasers with frequency disorder [68]. With increasing coupling, the eigenstates are no longer localized to individual lasers, but expand over multiple lasers. The eigenstate with the

highest eigenvalue will dominate lasing and its order parameter can be calculated. For selective sparse coupling, only the laser pairs with natural frequency differences above a threshold Δ_{th} are coupled with a constant coefficient, while the others are not coupled at all. With increasing Δ_{th}, the network connectivity χ decreases. The eigenstates can be compared with those of randomly connected networks with the same value of connectivity χ. With increasing χ, the order parameter of the dominant supermode increases much more quickly for selective coupling than random coupling. The lasers in the supermode oscillate in phase, but their amplitudes are not identical. The qualitative agreement with the LK simulation results suggest that the linear coupling matrix determines the supermode structure, which in term dictates laser synchronization. However, this simple model cannot predict the destabilization of synchronization at even stronger coupling where the coupled lasers chaotically hop between multiple supermodes [69, 70].

3.2. Effective thermodynamic potential for the laser network

For a more quantitative understanding, we develop a thermodynamic potential framework (see Sec. 4 in SI) to uncover the universal optimal sparse network structure that enables frequency- and phase-synchronized steady states in disordered diode laser systems. In particular, by expanding the LK equations near the synchronized steady state, we derive the generalized time-delayed Kuramoto model [71] with an additional phase shift $\phi \equiv \tan^{-1}\alpha + \omega_0\tau$:

$$\frac{d\Omega_i(t)}{dt} = \Delta_i - \sqrt{1+\alpha^2}\sum_{j=1}^{M} K_{ij}\sin[\Omega_i(t) - \Omega_j(t-\tau) + \phi], \tag{4}$$

where $\Omega_i(t)$ is the phase term of the electric field. With time-delay-induced phase differences

$$\eta_i \approx \Omega_i(t) - \Omega_i(t-\tau), \tag{5}$$

and assuming slow temporal phase evolution such that $\eta_i(t)/\tau \approx [\dot{\Omega}_i(t) + \dot{\Omega}_i(t-\tau)]/2$, the network dynamics can be reformulated as a gradient flow governed by an effective thermodynamic potential $U(\eta_i)$:

$$U(\eta_i(t)) = \eta_i^2(t) - 2\tau\Delta_i\eta_i(t) - 2\tau\sqrt{1+\alpha^2}k_i^{\text{in}}\cos[\eta_i(t) + \phi], \tag{6}$$

and $k_i^{\text{in}} \equiv \sum_{j=1}^{M} K_{ij}$ denotes the intrinsic coupling strength coming from other lasers to the i-th laser. This expression generalizes the result for a single laser [72]: $U(\nu(t)) = \nu^2(t) - 2\tau\sqrt{1+\alpha^2}\gamma\cos[\nu(t) + \phi]$, where γ is the self-coupling strength and $\nu(t) \equiv \Omega(t) - \Omega(t-\tau)$. The thermodynamic potential in Eq. (6) indicates that the effective coupling strength $\mathbb{K}_i \equiv \tau\sqrt{1+\alpha^2}k_i^{\text{in}}$ is governed by the time delay τ, the linewidth enhancement factor α (responsible for amplitude–phase coupling), and the intrinsic coupling strength k_i^{in} (or γ for a single laser).

The variational principle stipulates that the system's final dynamical steady state should settle at the local minimum of the potential. These local minima of $U(\eta_i(t))$ can be determined through the first and second derivatives with respect to $\eta_i(t)$:

$$\frac{dU(\eta_i(t))}{d\eta_i(t)} = \eta_i(t) - \tau\Delta_i + \mathbb{K}_i\sin[\eta_i(t) + \phi] = 0, \tag{7}$$

$$\frac{d^2U(\eta_i(t))}{d\eta_i^2(t)} = 1 + \mathbb{K}_i\cos[\eta_i(t) + \phi] > 0. \tag{8}$$

Setting $\omega_0\tau \equiv 2k\pi$, Eqs. (7) and (8) can be further simplified as

$$\eta_i - \mathbb{F}_i = -\mathbb{K}_i\sin(\eta_i + \phi), \tag{9}$$

$$1 + \mathbb{K}_i\cos(\eta_i + \phi) > 0, \tag{10}$$

where $\mathbb{F}_i \equiv \tau\Delta_i$ denotes the effective detuning, and the constant phase shift is defined as $\phi \equiv \mathrm{mod}(\tan^{-1}\alpha + \omega_0\tau, 2\pi) \approx 0.4\pi$. The solutions in (9) and (10) provide the steady steate solutions for each laser i. From the definition of the time-delayed phase difference in (5), the steady state solutions are related to the final frequencies:

$$\eta_i^*(t) \approx \Omega_i^{\mathrm{fit}} \times \tau + \varphi_i(t) - \varphi_i(t-\tau), \tag{11}$$

when $\Omega_i(t) = \Omega_i^{\mathrm{fit}} \times t + \varphi_i(t)$ and $\Omega_i(t-\tau) = \Omega_i^{\mathrm{fit}} \times (t-\tau) + \varphi_i(t-\tau)$. In the ideal case of complete synchronization, the solutions of η_i become independent of the laser index i and reduce to

$$\eta^* \approx \Omega^{\mathrm{fit}}\tau = 2\pi f_{\mathrm{final}}\tau, \tag{12}$$

in the regime where $\varphi_i(t) \approx \varphi_i(t-\tau)$, an approximation that is well justified in the numerical simulations.

3.3. *Understanding why sparse networks outperform homogeneous all-to-all coupling*

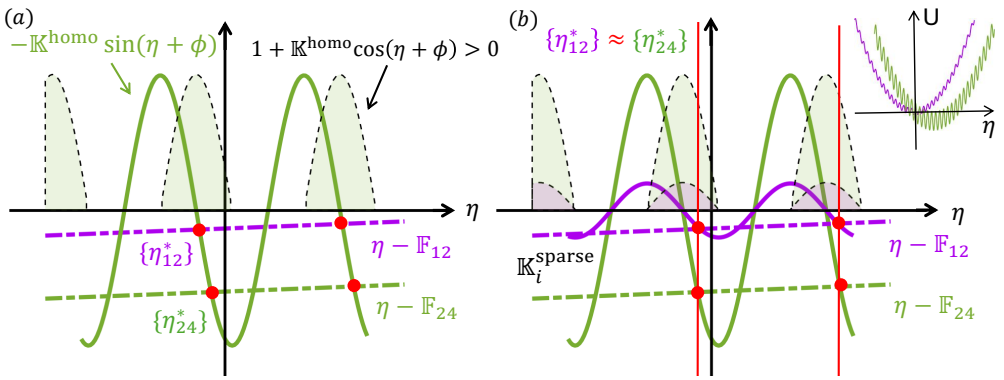

Fig. 5. Understanding synchronization in sparse networks. (a), (b) Schematic illustrations of steady-state selection from the potential landscape for different lasers under homogeneous all-to-all coupling and sparse coupling, respectively. The cross intersections of Eq. (9) are marked by the red dots in panels (a) and (b). These intersections fall within the light-shaded region that satisfies Eq. (10). Together, they define the steady-state solution sets $\{\eta_{12}^*\}$ and $\{\eta_{24}^*\}$. These solutions correspond to two representative effective detunings, $\mathbb{F}_{12}$ and $\mathbb{F}_{24}$ associated with the 12-th and 24-th lasers, respectively. The green and purple oscillatory curves represent stronger and weaker effective coupling strengths. The inset in (b) shows the effective thermodynamic potential in (6), consisting of a parabolic term and an oscillatory sinusoidal component. A smaller effective coupling $\mathbb{K}_i^{\mathrm{sparse}}$ produces a smoother potential with fewer steady-state solutions.

Based on the thermodynamic potential theory, the effective potentials for the homogeneous all-to-all coupling and the sparse coupling are given by:

$$U^{\mathrm{homo}}(\eta_i(t)) = \eta_i^2(t) - 2\tau\Delta_i\eta_i(t) - 2\mathbb{K}^{\mathrm{homo}}\cos[\eta_i(t)+\phi],$$
$$U^{\mathrm{sparse}}(\eta_i(t)) = \eta_i^2(t) - 2\tau\Delta_i\eta_i(t) - 2\mathbb{K}_i^{\mathrm{sparse}}\cos[\eta_i(t)+\phi],$$

Here, the effective couplings are defined as $\mathbb{K}^{\mathrm{homo}} \equiv \tau\sqrt{1+\alpha^2}\kappa(M-1)$, and $\mathbb{K}_i^{\mathrm{sparse}} \equiv \tau\sqrt{1+\alpha^2}\xi_i\kappa^f$, corresponding to the homogeneous and sparse networks, respectively. In the

homogeneous all-to-all case, $k^{in} = \sum_{j=1}^{M} K_{ij} = \kappa(M-1)$ is independent of the laser index i. In contrast, for the sparse network, $k_i^{in} = \sum_{j=1}^{M} K_{ij} = \xi_i \kappa^f$, where ξ_i denotes the total number of connected links for the i-th laser, and $\kappa^f = 1\, ns^{-1}$ is introduced to explicitly retain the physical units of coupling strength.

The total number of connected links for each laser is distributed non-uniformly over the laser index i, whereas in the homogeneous case it uniformly reaches the maximum value $\xi = M-1$. From (9), a smaller number of connected links corresponds to a reduced magnitude of the effective coupling $\mathbb{K}_i$, which in turn leads to fewer steady-state solutions for the i-th laser. Note that the overall coupling cost remains the same in both network types, $\sum_{ij} K_{ij} = \kappa M(M-1) = \chi M(M-1)\kappa^f$, yet the number of steady-state solutions for individual lasers can be substantially reduced in the sparse network. Consequently, the sparse network is able to significantly lower the total number of steady states, thereby enhancing overall stability.

In addition, a sparse network drives the final frequencies closer to each other, thereby promoting stronger synchronization. The cross intersections of Eq. (9), indicated by the red dots in Fig. 5, together with the light-shaded area satisfying Eq. (10), correspond to the final frequencies obtained from Eqs. (11) and (12). Figures 5(a) and 5(b) illustrate the fine structure of these solutions for the homogeneous all-to-all coupling and the sparse network, respectively. For two specific cases of effective detuning, with slopes biased by $\mathbb{F}_{12}$ and $\mathbb{F}_{24}$, a lower effective coupling leads to a smaller sinusoidal oscillation amplitude, emphasized by the purple curve compared with the green curve in Fig. 5(b). This tunable amplitude allows the final solution η^* and thus the final frequency, to align more closely with each other—effectively compensating for frequency disorder and yielding nearly identical final frequencies. In contrast, the homogeneous all-to-all coupling shown in Fig. 5(a) cannot achieve this adjustment due to its uniform effective coupling.

3.4. Understanding connectivity scaling and emergence of hub structure

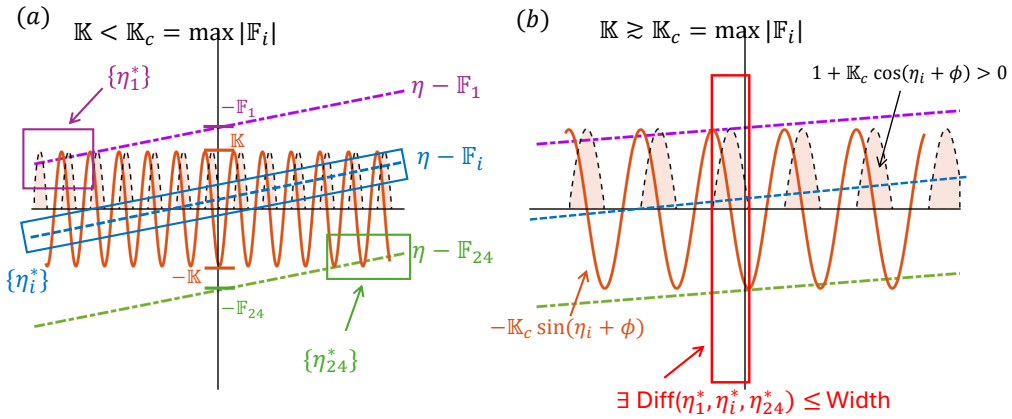

Fig. 6. Schematic of the critical effective coupling in the homogenous all-to-all coupling. (a) Effective coupling $\mathbb{K}$ below the critical value $\mathbb{K}_c$. (b) Effective coupling $\mathbb{K}$ around the critical value $\mathbb{K}_c$. The rectangular regions in (a) indicate the steady-state solution sets for the corresponding effective detuning $\mathbb{F}_i$. The red rectangular region in (b) highlights the first nearly synchronized state that emerges at the critical effective coupling, where the maximum frequency difference between lasers is around the width of the region satisfying $d^2U/d\eta^2 > 0$. The remaining notation follows Fig. 5.

For the homogenous all-to-all coupling, there exists a critical effective coupling strength that first enables the formation of a single, nearly synchronized steady state across all lasers,

consistent with previous work [60]. For $M = 24$, the frequency detunings are ordered as $\Delta_1 \leq \Delta_2 \leq \cdots \leq \Delta_{24}$. In this case, the effective detunings $\mathbb{F}_1$ and $\mathbb{F}_{24}$ define the boundaries of the steady-state solution structure, as shown in Fig. 6. When the effective coupling is too small, i.e., $\mathbb{K} < \mathbb{K}_c = \max|\mathbb{F}_i|$, the steady state solution sets $\{\eta_1^*\}$ and $\{\eta_{24}^*\}$ remain well separated. In this regime, intermediate detuning values $\mathbb{F}_i$ may yield solutions $\{\eta_i^*\}$ that lie close to $\{\eta_1^*\}$, but not to $\{\eta_{24}^*\}$, and conversely. As a result, only partial synchronization among the lasers is achieved. When the effective coupling approaches the critical value $\mathbb{K} \gtrsim \mathbb{K}_c = \max|\mathbb{F}_i|$, the steady-state solutions develop an overlap region encompassing all lasers, as indicated by the red rectangular region in Fig. 6(b). Since each steady-state solution η^* corresponds to a final frequency, the maximum frequency differences among the lasers in this region are bounded by the width of the region where $d^2U/d\eta^2 > 0$. This indicates that all lasers are nearly synchronized.

For the sparse network, the effective coupling depends on the laser index i, and each laser has its own critical value associated with the emergence of the hub structure. This behavior contrasts with that of the homogeneous all-to-all case. The effective coupling of each laser i is given by $\mathbb{K}_i^{\text{sparse}} \equiv \tau\sqrt{1+\alpha^2}\xi_i\kappa^f$. As shown in Fig. 5(b), achieving nearly identical steady-state solution sets requires the effective coupling of each laser to be comparable to its corresponding effective detuning as $\mathbb{K}_i^{\text{sparse}} \gtrsim |\mathbb{F}_i| = \tau|\Delta_i|$. Thus, for an arbitrary laser, the number of connections per laser ξ_i must exceed a threshold set by the local detuning, i.e., $\xi_i > |\Delta_i|/(\kappa^f\sqrt{1+\alpha^2})$, which is consistent with the observed hub topology where higher detuning demands more connections, as shown in Fig. 4(d). Consistently, the necessity of the hub structure can also be directly inferred from the Kuramoto model (see Sec. 5 in SI).

There also exists an overall expected critical value in the sparse network, which gives rise to the connectivity scaling law. The total number of connected links per laser ξ_i is related to the connectivity by $\sum_{i=1}^{M}\xi_i = \chi M(M-1)$. So, the expected effective coupling in our sparse network is $\langle\mathbb{K}^{\text{sparse}}\rangle = \sum_{i=1}^{M}\mathbb{K}_i^{\text{sparse}}/M = \tau\sqrt{1+\alpha^2}\chi(M-1)\kappa^f$. In the sparse network, the expected critical effective coupling is statistically close to the maximum effective detuning, $\langle\mathbb{K}_c^{\text{sparse}}\rangle \approx \max|\mathbb{F}_i| = \tau|\Delta_0|$ with the maximum detuning magnitude $|\Delta_0|$. Accordingly, the critical connectivity scales as $\chi_c \approx |\Delta_0|/[\kappa^f(M-1)\sqrt{1+\alpha^2}]$. The critical connectivity scales inversely with the laser size by $\chi_c \propto 1/(M-1)$ as derived from the nearly synchronized steady-state solutions of the effective thermodynamic potential. This scaling is consistent with the connectivity resonance, where the optimal connectivity follows $\chi^* \propto 1/(M-1)$.

Actually, the optimal connectivity is slightly higher than the critical connectivity, i.e., $\chi^* > \chi_c$. In the intermediate regime $\chi \in [\chi_c, \chi^*]$, multiple near-synchronized steady-state solutions are created. The dynamics gradually evolve from steady states to quasiperiodic motion—remaining stable but with reduced stability. At $\chi = \chi^*$, the onset of chaos suppresses the synchronization measure, as shown in Figs. 3(a) and 3(b). For example, the critical connectivity is $\chi_c \approx 0.26$ for $|\Delta_0| = 30$ rad/ns and $M = 24$. These bounds agree with the numerically revealed synchronization resonances under frequency disorder (Sec. 2 in SI), where all synchronization peaks occur within the connectivity range of approximately 0.3 to 0.4.

Furthermore, the final dynamic frequency, quantized as $\bar{f}_{\text{final}} = N/\tau$, satisfies the existence of a local minimum in the effective potential. Since the phase offset $\phi \equiv \text{mod}(\tan^{-1}\alpha + \omega_0\tau, 2\pi) \approx 0.4\pi < 0.5\pi$ [Fig. 5(b)], the quantized frequency in Fig. 2(d) always satisfies the stability condition $1 + \mathbb{K}_i\cos(2\pi\bar{f}_{\text{final}}\tau + \phi) > 0$ because $\cos\phi > 0 > -1/\mathbb{K}_i$. Given that $\alpha = 5$ and $\omega_0\tau = 2N\pi$, the resulting phase shift ϕ statistically favors negative values of η which are closer to the mean of the initial frequency distribution. As a result, the intersections in the potential landscape are biased toward negative η^*, producing a statistical preference for negative dynamic frequencies—that is, the final dynamic frequency tends to lie below the mean of the initial frequency distribution—consistent with the behavior observed in Fig. 2(d).

4. Discussion and conclusion

We have checked numerically that the synchronization behavior remains consistent with and without noise. While noise-free results are presented in the main text, the robustness of synchronization against dynamic and initial-state noise is detailed in Sec. 6A in SI. The selectively-coupled networks identified by the island-based genetic algorithm also exhibit robustness to perturbations in laser frequency detuning, coupling strength, and pump rate, highlighting the diversity and resilience of the genetic-algorithm landscape, as detailed in Sec. 6B and 6C in SI.

The island-based genetic algorithm constructs the optimal sparse networks by adaptively varying the number of connected links per laser ξ_i to compensate for the frequency disorder. Beyond disorder compensation, sparsity also reduces the overall coupling cost $\sum_{ij} K_{ij}$, suppressing multistability and promoting robust frequency- and phase-synchronized dynamics. The critical coupling strength in the classical Kuramoto model with homogeneous all-to-all coupling has been well characterized [73–75]. Here, we have generalized the analysis by incorporating the linewidth enhancement factor, time delay, and sparse coupling, and reformulate the critical bound from a physical perspective using a thermodynamic potential framework, as detailed in Secs. 4 and 5 in SI.

With different initial coupling configurations, the genetic algorithm-optimized network structures can exhibit small variations. However, the key features such as the hub lasers remains the same. In the sparse network, the lasers with small frequency detuning do not need to couple directly, as their indirect coupling through other lasers is already sufficient for synchronization. With increasing number of lasers M, the optimized networks become even more sparse, i.e., more laser pairs do not couple directly, since there are more indirect coupling paths through other lasers. The optimal connectivity χ^* scales as $\chi^* \propto 1/(M-1)$, indicating that the coupling cost increases linearly with the laser size as $\sum_{ij} K_{ij} \propto M$. Such linear scaling, instead of quadratic scaling with M, facilitates large-scale synchronization.

In summary, this work establishes a foundational theoretical framework for the emergence and scaling of sparse networks and hub structures for almost perfect synchronization. It provides a principled approach for designing scalable, cost-effective networks that sustain robust frequency and phase synchronization, along with a stable continuous-wave steady state, even under significant frequency disorder.

Funding. This work was supported by the Office of Naval Research under Grant No. N00014-24-1-2548.

Acknowledgment.

Disclosures. The authors declare no conflicts of interest.

Data Availability. Data underlying the results presented in this paper are not publicly available at this time but may be obtained from the authors upon reasonable request.

Supplemental document. See Supplement 1(link) for supporting content.

References

1. L. M. Pecora and T. L. Carroll, "Synchronization in chaotic systems," Phys. Rev. Lett. **64**, 821 (1990).
2. A. APikovsky, M. Rosenblum, and J. Kurths, *Synchronization: A universal concept in nonlinear sciences* (Cambridge University Press, 2001).
3. T. Nishikawa, A. E. Motter, Y.-C. Lai, and F. C. Hoppensteadt, "Heterogeneity in oscillator networks: Are smaller worlds easier to synchronize?" Phys. Rev. Lett. **91**, 014101 (2003).
4. A. Arenas, A. Díaz-Guilera, J. Kurths, *et al.*, "Synchronization in complex networks," Phys. Rep. **469**, 93–153 (2008).
5. J. D. Hart, Y. Zhang, R. Roy, and A. E. Motter, "Topological control of synchronization patterns: Trading symmetry for stability," Phys. Rev. Lett. **122**, 058301 (2019).
6. Y. Sugitani, Y. Zhang, and A. E. Motter, "Synchronizing chaos with imperfections," Phys. Rev. Lett. **126**, 164101 (2021).
7. T. Nishikawa and A. E. Motter, "Symmetric states requiring system asymmetry," Phys. Rev. Lett. **117**, 114101 (2016).

8. M. Nixon, M. Fridman, E. Ronen, *et al.*, "Controlling synchronization in large laser networks," Phys. Rev. Lett. **108**, 214101 (2012).
9. N. Nair, E. Bochove, and Y. Braiman, "Phase-locking of arrays of weakly coupled semiconductor lasers," Opt. Exp. **26**, 20040–20050 (2018).
10. T. Mihana, K. Fujii, K. Kanno, *et al.*, "Laser network decision making by lag synchronization of chaos in a ring configuration," Opt. Express **28**, 40112–40130 (2020).
11. N. Nair, K. Hu, M. Berrill, *et al.*, "Using disorder to overcome disorder: A mechanism for frequency and phase synchronization of diode laser arrays," Phys. Rev. Lett. **127**, 173901 (2021).
12. L. Zhang, W. Pan, L. Yan, *et al.*, "Strong cluster synchronization in complex semiconductor laser networks with time delay signature suppression," Opt. Express **30**, 30727–30738 (2022).
13. L. Zhang, L. Su, S. Li, *et al.*, "Regulation of cluster synchronization in multilayer networks of delay coupled semiconductor lasers with the use of disjoint layer symmetry," Opt. Express **32**, 1123–1134 (2024).
14. J. Katz, E. Kapon, C. Lindsey, *et al.*, "Phase-locked semiconductor laser array with separate contacts," Appl. Phys. Lett. **43**, 521–523 (1983).
15. L. Goldberg and J. Weller, "Single lobe operation of a 40-element laser array in an external ring laser cavity," Appl. Phys. Lett. **51**, 871–873 (1987).
16. D. Botez, L. Mawst, and G. Peterson, "Resonant leaky-wave coupling in linear arrays of antiguides," Electron. Lett. **24**, 1328–1330 (1988).
17. M. Orenstein, E. Kapon, J. Harbison, *et al.*, "Large two-dimensional arrays of phase-locked vertical cavity surface emitting lasers," Appl. Phys. Lett. **60**, 1535–1537 (1992).
18. R.-d. Li and T. Erneux, "Preferential instability in arrays of coupled lasers," Phys. Rev. A **46**, 4252 (1992).
19. G. Kozyreff, A. Vladimirov, and P. Mandel, "Global coupling with time delay in an array of semiconductor lasers," Phys. Rev. Lett. **85**, 3809 (2000).
20. Y. Liu and Y. Braiman, "Synchronization of high-power broad-area semiconductor lasers," IEEE J. Sel. Top. Quantum Electron. **10**, 1013–1024 (2004).
21. B. Liu and Y. Braiman, "Coherent beam combining of high power broad-area laser diode array with near diffraction limited beam quality and high power conversion efficiency," Opt. Express **21**, 31218–31228 (2013).
22. A. Argyris, M. Bourmpos, and D. Syvridis, "Experimental synchrony of semiconductor lasers in coupled networks," Opt. express **24**, 5600–5614 (2016).
23. M. Pflüger, D. Brunner, T. Heuser, *et al.*, "Injection locking and coupling the emitters of large VCSEL arrays via diffraction in an external cavity," Opt. Express **31**, 8704–8713 (2023).
24. Z. Song, R. Sun, F. He, *et al.*, "Phase-locked high-brightness interband cascade laser array with multimode interferometer couplers," Opt. Lett. **49**, 6197–6200 (2024).
25. S. Longhi and L. Feng, "Invited article: mitigation of dynamical instabilities in laser arrays via non-hermitian coupling," APL Photonics **3** (2018).
26. S. Xiang, Y. Han, H. Wang, *et al.*, "Zero-lag chaos synchronization properties in a hierarchical tree-type network consisting of mutually coupled semiconductor lasers," Nonlinear Dyn. **99**, 2893–2906 (2020).
27. S. Liu, N. Jiang, Y. Zhang, *et al.*, "Chaos synchronization based on cluster fusion in asymmetric coupling semiconductor lasers networks," Opt. Express **29**, 16334–16345 (2021).
28. Y. G. Liu, Y. Wei, O. Hemmatyar, *et al.*, "Complex skin modes in non-hermitian coupled laser arrays," Light Sci. Appl. **11**, 336 (2022).
29. Z. Gao, X. Qiao, M. Pan, *et al.*, "Two-dimensional reconfigurable non-hermitian gauged laser array," Phys. Rev. Lett. **130**, 263801 (2023).
30. M. P. Hokmabadi, N. S. Nye, R. El-Ganainy, *et al.*, "Supersymmetric laser arrays," Science **363**, 623–626 (2019).
31. X. Qiao, B. Midya, Z. Gao, *et al.*, "Higher-dimensional supersymmetric microlaser arrays," Science **372**, 403–408 (2021).
32. M. A. Bandres, S. Wittek, G. Harari, *et al.*, "Topological insulator laser: Experiments," Science **359**, eaar4005 (2018).
33. A. Dikopoltsev, T. H. Harder, E. Lustig, *et al.*, "Topological insulator vertical-cavity laser array," Science **373**, 1514–1517 (2021).
34. A. E. Motter, C. Zhou, and J. Kurths, "Enhancing complex-network synchronization," Eur. Lett. **69**, 334 (2005).
35. A. E. Motter, C. Zhou, and J. Kurths, "Network synchronization, diffusion, and the paradox of heterogeneity," Phys. Rev. E. **71**, 016116 (2005).
36. C. Zhou, A. E. Motter, and J. Kurths, "Universality in the synchronization of weighted random networks," Phys. Rev. Lett. **96**, 034101 (2006).
37. T. Nishikawa and A. E. Motter, "Synchronization is optimal in nondiagonalizable networks," Phys. Rev. E **73**, 065106 (2006).
38. T. Nishikawa and A. E. Motter, "Maximum performance at minimum cost in network synchronization," Phys. D: Nonlinear Phenom. **224**, 77–89 (2006).
39. L. Huang, K. Park, Y.-C. Lai, *et al.*, "Abnormal synchronization in complex clustered networks," Phys. Rev. Lett. **97**, 164101 (2006).
40. X. Wang, Y.-C. Lai, and C. H. Lai, "Enhancing synchronization based on complex gradient networks," Phys. Rev. E **75**, 056205 (2007).

41. Z. Duan, G. Chen, and L. Huang, "Complex network synchronizability: Analysis and control," Phys. Rev. E **76**, 056103 (2007).
42. Y. Gu and J. Sun, "Altering synchronizability by adding and deleting edges for scale-free networks," Phys. A **388**, 3261–3267 (2009).
43. T. Nishikawa and A. E. Motter, "Network synchronization landscape reveals compensatory structures, quantization, and the positive effect of negative interactions," Proc. Natl. Acad. Sci. U.S.A. **107**, 10342–10347 (2010).
44. B. Ravoori, A. B. Cohen, J. Sun, *et al.*, "Robustness of optimal synchronization in real networks," Phys. Rev. Lett. **107**, 034102 (2011).
45. Y. Zhang and A. E. Motter, "Identical synchronization of nonidentical oscillators: when only birds of different feathers flock together," Nonlinearity **31**, R1–R23 (2018).
46. Y. Zhang, J. L. Ocampo-Espindola, I. Z. Kiss, and A. E. Motter, "Random heterogeneity outperforms design in network synchronization," Proc. Natl. Acad. Sci. **118**, e2024299118 (2021).
47. M. Brede, "Synchrony-optimized networks of non-identical kuramoto oscillators," Phys. Lett. A **372**, 2618–2622 (2008).
48. M. Brede, "Locals vs. global synchronization in networks of non-identical kuramoto oscillators," Eur. Phys. J. B **62**, 87–94 (2008).
49. L. Buzna, S. Lozano, and A. Díaz-Guilera, "Synchronization in symmetric bipolar population networks," Phys. Rev. E **80**, 066120 (2009).
50. D. Kelly and G. A. Gottwald, "On the topology of synchrony optimized networks of a kuramoto-model with non-identical oscillators," Chaos **21** (2011).
51. S. Acharyya and R. Amritkar, "Synchronization of coupled nonidentical dynamical systems," Eur. Lett. **99**, 40005 (2012).
52. P. S. Skardal, D. Taylor, and J. Sun, "Optimal synchronization of complex networks," Phys. Rev. Lett. **113**, 144101 (2014).
53. M. Fazlyab, F. Dörfler, and V. M. Preciado, "Optimal network design for synchronization of coupled oscillators," Automatica **84**, 181–189 (2017).
54. L. Gil, "Optimally frequency-synchronized networks of nonidentical kuramoto oscillators," Phys. Rev. E **104**, 044211 (2021).
55. Y. Lei, X.-J. Xu, X. Wang, *et al.*, "A new criterion for optimizing synchrony of coupled oscillators," Chaos Solitons Fract. **168**, 113192 (2023).
56. A. Mihara, E. S. Medeiros, A. Zakharova, and R. O. Medrano-T, "Sparsity-driven synchronization in oscillator networks," Chaos **32** (2022).
57. D. Brunner and I. Fischer, "Reconfigurable semiconductor laser networks based on diffractive coupling," Opt. Lett. **40**, 3854–3857 (2015).
58. H. G. Winful and S. S. Wang, "Stability of phase locking in coupled semiconductor laser arrays," Appl. Phys. Lett. **53**, 1894–1896 (1988).
59. H. G. Winful and L. Rahman, "Synchronized chaos and spatiotemporal chaos in arrays of coupled lasers," Phys. Rev. Lett. **65**, 1575 (1990).
60. L.-L. Ye, N. Vigne, F.-Y. Lin, *et al.*, "Disorder-mediated synchronization resonance in coupled semiconductor lasers," (2025).
61. R. Lang and K. Kobayashi, "External optical feedback effects on semiconductor injection laser properties," IEEE J. Quantum Electron. **16**, 347–355 (1980).
62. I. Fischer, R. Vicente, J. M. Buldú, *et al.*, "Zero-lag long-range synchronization via dynamical relaying," Phys. Rev. Lett. **97**, 123902 (2006).
63. J. Zamora-Munt, C. Masoller, J. Garcia-Ojalvo, and R. Roy, "Crowd synchrony and quorum sensing in delay-coupled lasers," Phys. Rev. Lett. **105**, 264101 (2010).
64. M. Bourmpos, A. Argyris, and D. Syvridis, "Sensitivity analysis of a star optical network based on mutually coupled semiconductor lasers," J. Light. Technol. **30**, 2618–2624 (2012).
65. E. Cohen, M. Rosenbluh, and I. Kanter, "Phase transition in crowd synchrony of delay-coupled multilayer laser networks," Opt. Express **20**, 19683–19689 (2012).
66. M. Bourmpos, A. Argyris, and D. Syvridis, "Analysis of the bubbling effect in synchronized networks with semiconductor lasers," IEEE Photon. Technol. Lett. **25**, 817–820 (2013).
67. M. Bourmpos, A. Argyris, and D. Syvridis, "Coupled semiconductor laser network topologies for efficient synchronization," in *Physics and Simulation of Optoelectronic Devices XXIII,* vol. 9357 (SPIE, 2015), pp. 200–209.
68. N. Nair, E. Bochove, and Y. Braiman, "Almost perfect in-phase and anti-phase chaotic and periodic phase synchronization in large arrays of diode lasers," Opt. Commun. **430**, 104–111 (2019).
69. R. L. Davidchack, Y.-C. Lai, A. Gavrielides, and V. Kovanis, "Chaotic transitions and low-frequency fluctuations in semiconductor lasers with optical feedback," Phys. D **145**, 130–143 (2000).
70. M. C. Soriano, J. García-Ojalvo, C. R. Mirasso, and I. Fischer, "Complex photonics: Dynamics and applications of delay-coupled semiconductors lasers," Rev. Mod. Phys. **85**, 421–470 (2013).
71. M. S. Yeung and S. H. Strogatz, "Time delay in the kuramoto model of coupled oscillators," Phys. Rev. Lett. **82**, 648 (1999).
72. D. Lenstra, "Statistical theory of the multistable external-feedback laser," Opt. Commun. **81**, 209–214 (1991).

73. N. Chopra and M. W. Spong, "On exponential synchronization of Kuramoto oscillators," IEEE Trans. Autom. Control. **54**, 353–357 (2009).
74. A. Jadbabaie, N. Motee, and M. Barahona, "On the stability of the Kuramoto model of coupled nonlinear oscillators," in *Proc. Amer. Control Conf. (ACC), 2004,* vol. 5 (IEEE, 2004), pp. 4296–4301.
75. F. Dörfler and F. Bullo, "On the critical coupling for kuramoto oscillators," SIAM J. Appl. Dyn. Syst. **10**, 1070–1099 (2011).

This document provides supplementary information for "Optimal sparse networks for synchronization of semiconductor lasers." In Sec. 1, we present the phenomenon of synchronization resonance in inhomogeneous networks and compare it with that arising in homogeneous all-to-all coupled networks, demonstrating that the resonance is robust to the network structure. In Sec. 2, we examine the phenomenon of connectivity resonance in sparse networks in more detail and explain how genetic algorithm can be used to find the optimal network structure (in Sec. B). We demonstrate that the optimized networks show reduced preference for connections between lasers with close frequency detuning. In Sec. 3, we simplify the Lang–Kobayashi equations to obtain a network of coupled linear oscillators to offer intuition for the optimal sparse network structure, providing a quick guide for experimental interpretation. In Sec. 4, we provide a more quantitative understanding by analytically deriving the effective thermodynamic potential from the full Lang–Kobayashi equations for the system of coupled-lasers with time delay due to an external-cavity feedback. In Sec. 5, we provide a detailed physical understanding of the optimal sparse network structure, including the emergence of hub structures and the scaling law of optimal connectivity in comparison with homogeneous all-to-all coupled networks. In Sec. 6, we investigate the robustness of synchronization in sparse networks against dynamic noise, initial-state perturbations, and random variations in frequency detuning, coupling strength, pump rate, and coupling ramping. Furthermore, we mix multiple optimized sparse coupling matrices to explore the optimization landscape of the genetic algorithm to address the issue of landscape robustness.

1. SYNCHRONIZATION RESONANCE IN INHOMOGENEOUS ALL-TO-ALL COUPLING

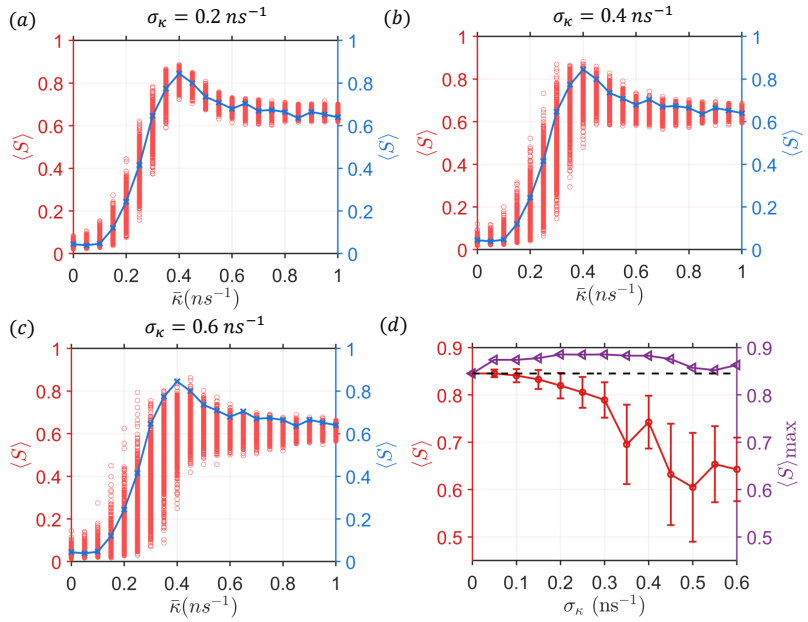

Fig. S1. Robust synchronization resonance with slightly enhanced performance in inhomogeneous all-to-all coupled diode laser networks. The nodal coupling is given by $K_{ij} = [\bar{\kappa} + \sigma_\kappa \mathcal{N}(0,1)]\,(1-\delta_{ij})$ with $\mathcal{N}(0,1)$ being a normalized Gaussian random variable. (a-c) Synchronization measure $\langle S\rangle$ versus $\bar{\kappa}$ for $\sigma_\kappa = 0.2\,\mathrm{ns}^{-1}$, $0.4\,\mathrm{ns}^{-1}$, and $0.6\,\mathrm{ns}^{-1}$, respectively, for $M = 24$, where the blue curve represents the baseline from the homogeneous all-to-all coupled network with $K_{ij} = \bar{\kappa}(1-\delta_{ij})$. The coupling strength is scanned over the range $\bar{\kappa} \in [0,1]\,\mathrm{ns}^{-1}$ with a step size of $0.05\,\mathrm{ns}^{-1}$. (d) Mean values and standard deviations of the randomly sampled synchronization measure $\langle S\rangle$ at the resonance peak $\bar{\kappa}^* = 0.4\,\mathrm{ns}^{-1}$ versus the perturbation strength σ_κ. The corresponding peak values of $\langle S\rangle_{\max}$ as a function of σ_κ are displayed on the right. For reference, the horizontal dashed line marks the maximum $\langle S\rangle$ obtained in homogeneous all-to-all networks, providing a baseline for comparison.

In homogeneous, all-to-all coupled diode laser networks, a synchronization resonance emerges.

The coupling matrix is defined as $K_{ij} = \kappa$ for $i \neq j$ and $K_{ii} = 0$, thereby eliminating self-feedback. Under frequency disorder, the synchronization measure $\langle S \rangle$ reaches a maximum at an optimal coupling strength, whereas in the absence of disorder this resonance disappears. A natural question arises: does synchronization resonance, as exemplified by the blue curves in Figs. S1(a–c), persist when the couplings become inhomogeneous? We find that deviations from homogeneous coupling preserve—and may even slightly enhance—the synchronization resonance.

To introduce coupling heterogeneity, we perturb the interaction strength as

$$\kappa \to \bar{\kappa} + \sigma_\kappa \mathcal{N}(0,1),$$

where $\bar{\kappa}$ denotes the baseline coupling and $\mathcal{N}(0,1)$ represents a normalized Gaussian random variable. For each perturbation level σ_κ, we generate 1000 independent realizations of the perturbed coupling matrices for every fixed value of $\bar{\kappa}$. Figures S1(a–c) present results for $M = 24$ lasers with frequency disorders $\Delta_i = 14 \times \mathcal{N}(0,1)$ rad/ns generated using the random seed `rng(1)`, a typical disorder configuration. The plots show the dependence of $\langle S \rangle$ on $\bar{\kappa}$ for $\sigma_\kappa = 0.2$ ns^{-1}, 0.4 ns^{-1}, and 0.6 ns^{-1}, respectively, with the blue curve serving as a reference for the homogeneous network. Despite the spread in $\langle S \rangle$ at each fixed $\bar{\kappa}$, synchronization resonance persists in all cases. Figure S1(d) summarizes the mean values and standard deviations of $\langle S \rangle$ at the resonance peak (left) and the corresponding peak values $\langle S \rangle_{\max}$ as a function of σ_κ (right). The horizontal dashed line marks the maximum $\langle S \rangle_{\max}$ obtained for the homogeneous, all-to-all coupled network. These results demonstrate that random variations in coupling strength can partially compensate for frequency disorder, thereby enhancing overall synchronization.

Based on the theoretical framework described in Sec. 5, inhomogeneous all-to-all coupling introduces small variations in the total coupling strength experienced by each laser. These variations can partially compensate for frequency disorder, thereby reducing the number of possible steady-state solutions. Consequently, the final laser frequencies become more closely aligned, resulting in more stable dynamics and a moderate enhancement of both frequency and phase synchronization.

2. OPTIMIZING SYNCHRONIZATION IN SPARSELY COUPLED DIODE-LASER NETWORKS

A. Connectivity resonance in synchronization

The all-to-all coupled diode-laser networks studied in Sec. 1 demonstrate that random inhomogeneous coupling can partially compensate for frequency disorder and thereby enhance synchronization. A different form of inhomogeneity arises from the network structure itself, specifically, through sparse coupling architectures. From an experimental standpoint, sparsely coupled laser networks offer practical advantages in implementation. As discussed in the main text, network sparsity is quantified by the connectivity $0 \leq \chi \leq 1$, defined as the fraction of nonzero entries in the coupling matrix normalized by the total number of possible links $M(M-1)$. The case $\chi = 1$ corresponds to all-to-all coupling. As χ increases from zero, synchronization attains a maximum at an optimal connectivity χ^*, giving rise to the phenomenon of connectivity resonance, as described in the main text. Here we provide additional results illustrating the emergence of this resonance, shown in Fig. S2.

In our simulations, following experimental considerations, the coupling matrix is constrained to be binary (entries are either 0 or 1), symmetric, and free of self-coupling (zero diagonal elements). For each connectivity level, we perform random sampling over 1000 sparse coupling configurations with different frequency disorder realizations. The resulting values of $\langle S \rangle$ are shown as yellow points in Figs. S2(a–i), corresponding to nine statistically independent realizations of the frequency disorder. In each panel, the green curve represents the homogeneous, all-to-all reference case.

For the homogeneous all-to-all network with coupling strength κ, the total intrinsic coupling per laser is

$$k^{\text{in}}_{\text{Homo}} = \sum_j K_{ij} = \kappa(M-1).$$

In the case of sparse binary coupling, the expected total coupling per laser is

$$k^{\text{in}}_{\text{Spa}} = \mathbb{E}[\sum_j K_{ij}] = \chi(M-1)\kappa^f$$

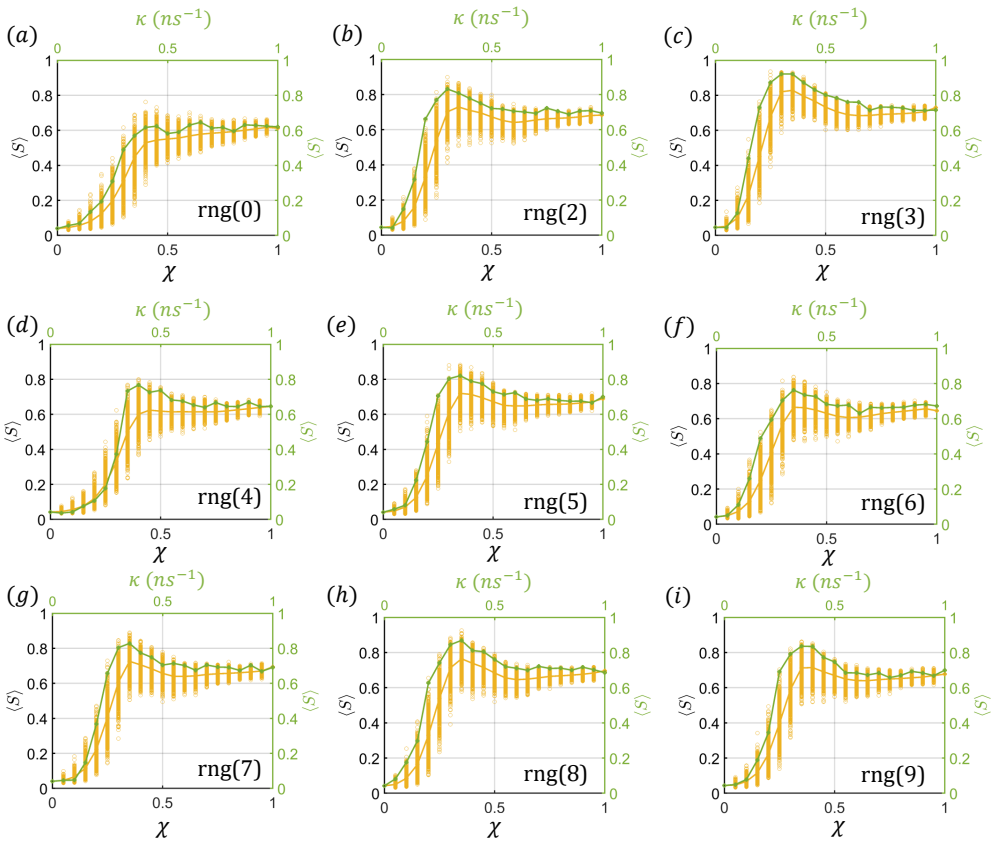

Fig. S2. Connectivity resonance in sparsely all-to-all coupled diode laser networks. Frequency disorder is modeled as Gaussian detuning, $\Delta_i = 14 \times \mathcal{N}(0,1)$ rad/ns, with nine independent realizations (panels a–i, random seeds `rng(0)`, `rng(2)`–`rng(9)`; `rng(1)` shown in Fig. 2(a) of the main text). In each panel, the green curve denotes the homogeneous all-to-all benchmark $K_{ij} = \kappa(1 - \delta_{ij})$, while 1000 yellow points per connectivity level represent randomly sampled sparse configurations, with the yellow curve indicating their average.

where $\kappa^f = 1, \mathrm{ns}^{-1}$. For a fixed total coupling per laser, there exists a one-to-one correspondence between κ and the connectivity χ. Remarkably, even with randomly sampled configurations, sparse networks can outperform the homogeneous all-to-all networks near the synchronization resonance region, as shown in Figs. S2(a–i). Furthermore, the synchronization peak κ^* observed in the homogeneous case statistically coincides with the optimal connectivity χ^* in sparse networks, indicating that the synchronization threshold is primarily determined by the total coupling per laser.

B. Exploiting island genetic algorithm to find optimal sparsely coupled networks

In Sec. A, we showed that Monte Carlo sampling of sparsely coupled configurations can yield networks exhibiting stronger frequency and phase synchronization than any homogeneous all-to-all network with the same total coupling cost K_{total} in the weak-coupling regime. This observation implies the existence of optimal sparse networks with enhanced synchronization, motivating the use of optimization methods such as genetic algorithms to identify such structures. To this end, we employ an island genetic algorithm, initialized at the connectivity level that produces the best synchronization performance in the Monte Carlo simulations, to discover coupling configurations with further improved synchronization.

The implementation of the island genetic algorithm for our network optimization problem proceeds as follows. A standard genetic algorithm is first applied to evolve a population of 200 candidate coupling matrices per generation. The optimization typically converges after approximately 200 generations. Each matrix is evaluated using the synchronization measure $\langle S \rangle$ as the fitness function. Parent matrices are selected via roulette-wheel selection, assigning

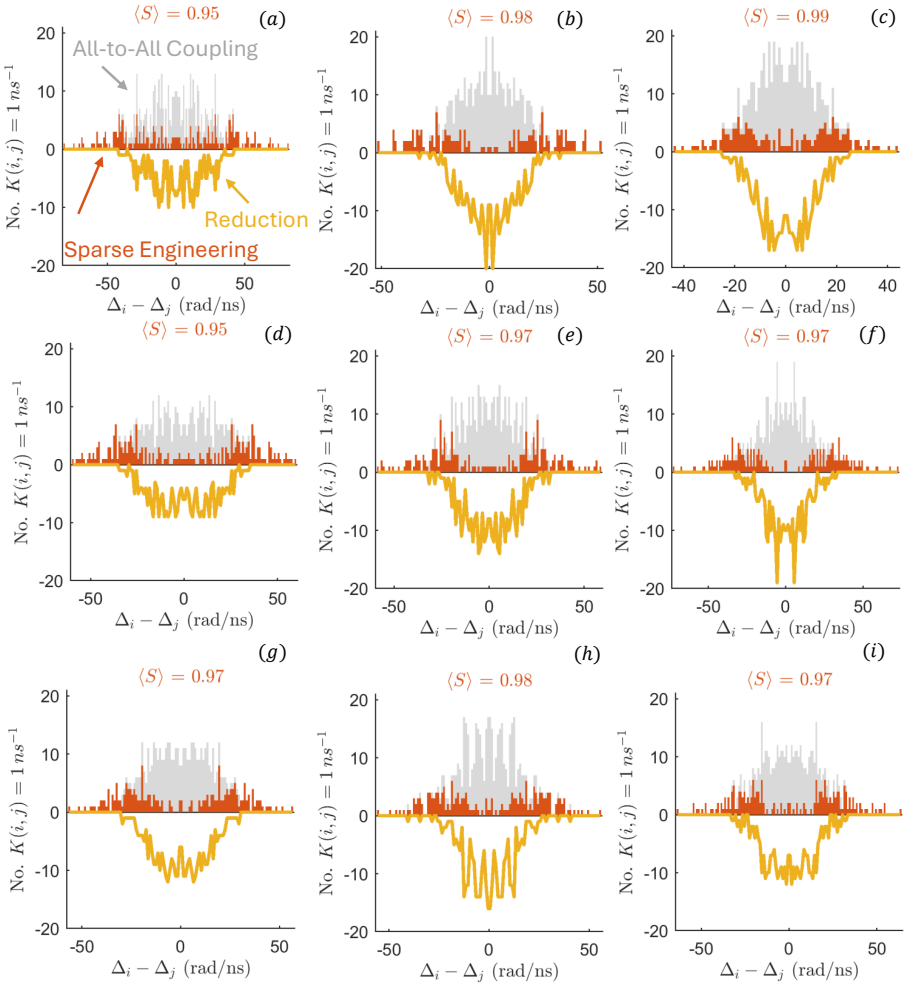

Fig. S3. Comparison of coupling characteristics in homogeneous all-to-all networks and in optimal sparse networks identified by an island genetic algorithm. Shown are the statistical distributions of the network couplings as a function of frequency detuning differences. Panels (a–i) correspond to random seeds `rng`(0) through `rng`(9), excluding `rng`(1) (already presented in the main text). The ordering of random seeds matches that in Fig. S2. To emphasize the effect of sparsity, the coupling strength is fixed at $\kappa = 1, \mathrm{ns}^{-1}$ for the homogeneous all-to-all case, while links are selectively removed using an island genetic algorithm to enhance synchronization. The removed connections indicate nonessential links. In each panel, the gray histogram shows the synchronization distribution for the homogeneous case $\langle S \rangle \approx 0.67$, averaged over all frequency disorder realizations), the orange histogram corresponds to the optimal sparse network, and the yellow histogram highlights the difference between the two.

higher selection probabilities to individuals with higher fitness. Crossover is then performed between selected parent pairs, with each pair generating two offspring. Edges shared between the parents are directly inherited, while the remaining edges are randomly assigned to preserve the total number of links and ensure the same structural constraints as the parents. Each offspring undergoes mutation at a fixed rate of 0.03, in which one randomly chosen link is removed and replaced by a new random connection elsewhere in the network. The top 8 high-performing individuals (elites) are preserved in each generation.

To promote diversity and avoid premature convergence to local optima, we implement a migration strategy across four independent islands, each containing 50 individuals. Every five generations, migration occurs sequentially: Island $1 \to 2$, $2 \to 3$, $3 \to 4$, and $4 \to 1$, where the worst-performing 5% of individuals on the receiving island are replaced by the elites migrating

from the source island. This island-based genetic algorithm framework enhances exploration of the optimization landscape while preserving the best-performing solutions, leading to robust identification of sparse coupling networks with optimal synchronization properties.

The patterns providing physical insight into the optimized sparse coupling matrices obtained from the island genetic algorithm are shown in Figs. S3(a–i) across different frequency disorder realizations corresponding to random seeds `rng`(0–9). These results reveal a characteristic structure in which couplings are suppressed between lasers with small frequency differences and preserved between those with large frequency separations. Consequently, the resulting histogram exhibits a dip near zero frequency difference and an overall parabolic shape. To isolate the effect of sparsity, coupling matrix elements for both the homogeneous all-to-all and optimized sparse configurations are constrained to binary values, either 0 or $1, \mathrm{ns}^{-1}$. Figures S3(a–i) present histograms quantifying the number of coupling elements with $K_{ij} = 1, \mathrm{ns}^{-1}$ within discrete intervals of the frequency differences $\Delta_i - \Delta_j$. In homogeneous all-to-all networks, all off-diagonal elements satisfy $K_{ij} = 1, \mathrm{ns}^{-1}$, so the histogram of K_{ij} versus $\Delta_i - \Delta_j$ directly reflects the statistical distribution of the frequency differences. As the frequencies follow a Gaussian distribution, the corresponding histogram (gray background in Fig. S3) also appears Gaussian-shaped, with a mean synchronization level $\langle S \rangle \approx 0.67$ averaged over all frequency disorder realizations. In contrast, the optimized sparse networks exhibit a marked reduction in couplings between lasers with small frequency detuning differences $\Delta_i - \Delta_j \to 0, \mathrm{rad/ns}$, while preferentially preserving connections among those with larger frequency separations. This trend is captured by the yellow curves in Fig. S3, which display a distinct dip near $\Delta_i - \Delta_j \to 0, \mathrm{rad/ns}$ and an overall parabolic profile across the full range of frequency differences. These results suggest that optimal sparse networks actively break the symmetric coupling pattern of the homogeneous configuration to exploit frequency heterogeneity: by linking more detuned lasers, the system balances coupling-induced locking and disorder-driven desynchronization, thereby creating an effective mechanism of structural adaptation that promotes stronger global coherence.

3. COUPLED NETWORK OF LINEAR OSCILLATORS

We examine whether sparse and selective coupling enables faster global phase and frequency synchronization, while requiring lower total coupling strength than conventional all-to-all or nearest-neighbor configurations. To build design intuition and isolate the effect of coupling topology from intrinsic laser nonlinearities, we model the system as a network of linearly coupled oscillators that represent the laser array:

$$\frac{dE_i(t)}{dt} = (i\Delta_i - \gamma)E_i(t) + \sum_{j \neq i}^{M} K_{ij} E_j(t), \tag{S1}$$

where $E_i(t)$ denotes the slowly varying complex field amplitude of laser i, and Δ_i is its detuning relative to a rotating frame at ω_0. Each cavity has a loss rate of $\gamma = 500, \mathrm{ns}^{-1}$. The coupling topology is specified by the symmetric, sparse, binary matrix *mathbbK*, whose off-diagonal elements represent the coupling strength between lasers i and j ($K_{ij} = K_{ji}$, either 0 or $\kappa = 1\ \mathrm{ns}^{-1}$); diagonal entries are set to zero to exclude self-feedback. The overall network connectivity is quantified as

$$\chi = \frac{1}{M(M-1)} \sum_{ij} K_{ij}/\kappa.$$

This linear system serves as a simplified representation of the Lang–Kobayashi model, neglecting gain dynamics, phase-amplitude coupling, and propagation delay. While it does not yield quantitative predictions, it provides clear intuition for designing coupling topologies.

The formal solution of Eq. (S1) can be expressed as $E_i^m(t) = v_i^m e^{\lambda^m t}$, where λ^m is generally a complex eigenvalue, i denotes the laser index ($i = 1, 2, \ldots, M$), and m denotes the eigenvalue index. Substituting this ansatz into Eq. (S1) gives

$$\lambda^m v_i^m = (i\Delta_i - \gamma)v_i^m + \sum_{j \neq i}^{M} K_{ij} v_j^m,$$

which leads to the eigenvalue equation

$$\sum_{j \neq i}^{M} A_{ij} v_j^m = \lambda^m v_i^m,$$

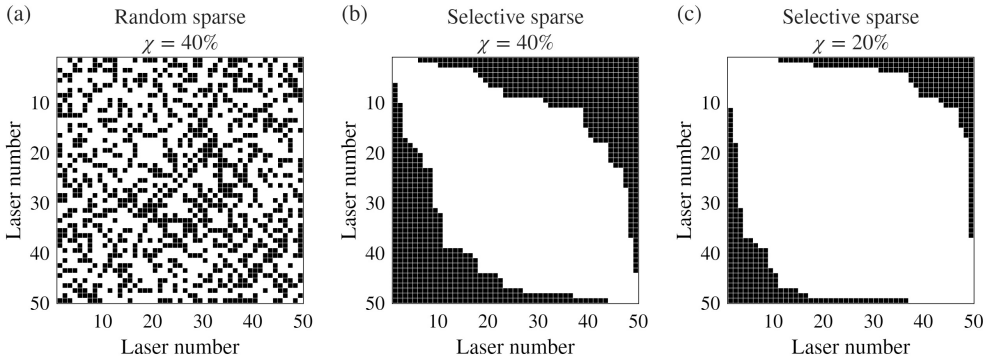

Fig. S4. Example of the different coupling matrix for an array of $M = 50$ lasers. The laser are ordered from the most negatively detuned (laser 1) to the most positively detuned (laser 50). A black square indicate a link with coupling strength $\kappa = 1$ ns^{-1}. (a) Random sparse matrix with a connectivity of $\chi = 40$ %. The link are symmetric and random distributed over all laser. (b) and (c) are example of the Selective sparse matrix for 40 % and 20 % connectivity respectively. In this configuration the most detuned laser are connected first until the required connectivity is achieved.

or equivalently, $\mathbb{A} \cdot \vec{v}^m = \lambda^m \vec{v}^m$. The matrix $\mathbb{A}$ takes the form

$$\mathbb{A} = \begin{bmatrix} (i\Delta_1 - \gamma) & K_{12} & \cdots & K_{1M} \\ K_{21} & \ddots & & \vdots \\ \vdots & & \ddots & K_{(M-1)M} \\ K_{M1} & \cdots & K_{M(M-1)} & (i\Delta_M - \gamma) \end{bmatrix}, \tag{S2}$$

which encodes both the coupling matrix K and the intrinsic dynamics of the individual oscillators, $(i\Delta_i - \gamma)$.

The eigenvalue spectrum λ^m and the corresponding eigenvectors $\vec{v}^m$ of the matrix $\mathbb{A}$ in Eq. Eq. (S2) determine the behavior of the network's "supermode" solutions. Because all eigenvalues possess negative real parts, the eigenvalue with the largest real component identifies the dominant or slowest-decaying supermode. Consequently, the analysis focuses on the corresponding eigenvector $\vec{v}^{m_{\max}}$, associated with the eigenvalue having the largest $\mathrm{Re}[\lambda^{m_{\max}}]$. For compactness, the field of laser i is written as $E_i(t) = v_i e^{\lambda t}$. The imaginary part of λ specifies the oscillation frequency of the collective mode.

Each field $E_i(t)$ carries both the intrinsic phase of laser i and a global phase contribution from $e^{\lambda t}$. The phase coherence among lasers is quantified using the synchronization order parameter

$$R = \frac{1}{M} \left| \sum_{i=1}^{M} e^{i \arg(v_i)} \right|,$$

in which the global phase of λ is excluded. The spatial intensity distribution is obtained from $|E_i(t)| = |v_i||e^{\lambda t}|$. Since $|e^{\lambda t}|$ is a common time-dependent factor, it can be omitted, yielding a time-independent intensity profile for the dominant supermode given by $|E_i| \sim |v_i|$.

To investigate how the dominant supermode attains a high degree of phase synchronization—specifically, how individual lasers within the network synchronize under varying coupling topologies—we simulate two types of sparse coupling configurations for laser arrays with sizes ranging from $M = 50$ to $M = 200$. The first configuration, referred to as the random sparse topology, is generated by randomly removing links from the full coupling matrix until the desired connectivity is achieved. The second configuration, termed the selective sparse topology, is obtained by progressively removing links between lasers with the smallest detuning values (see Fig. S4 for representative matrices). For each topology, the connectivity χ is varied from 6% to 50%, and simulations are performed over 100 realizations of laser frequency detuning drawn from a normal distribution with a standard deviation of $\sigma = 14$ rad/ns. In the random sparse

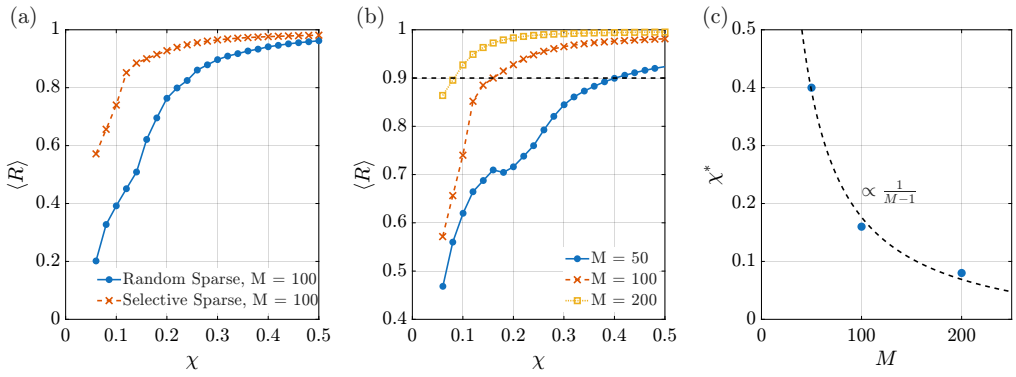

Fig. S5. Simulation results of the linear coupled network. (a) Average order parameter $\langle R \rangle$ of the dominant super-mode $\vec{v}^{m_{\max}}$ as a function of connectivity χ for $M = 100$ lasers array. The blue dot are for a random sparse matrix and the red cross for a selective one. (b) Comparison of the average order parameter as a function of connectivity for different number of laser in a selective sparse configuration. Blue dot is for $M = 50$, red cross $M = 100$ and yellow square for $M = 200$. The dashed black line is set to $\langle R \rangle = 0.9$ and used to define the critical connectivity χ^*. All results are the average of 100 normally distributed frequency realization with standard deviation of $\sigma = 14$ rad/ns. The Random sparse configuration is also average over 10 different random configuration. (c) Scaling of the critical connectivity χ^* as a function of the number of laser M in the array for a selective sparse configuration.

case, an additional ensemble average is conducted over 10 distinct random realizations of the coupling matrix.

Figure S5(a) compares the averaged synchronization order parameter $\langle R \rangle$ of the dominant supermode for both random and selective sparse configurations. The selective sparse topology achieves a highly synchronized state ($\langle R \rangle > 0.9$) at substantially lower connectivity ($\chi \sim 15\%$) than the random sparse network ($\chi \sim 30\%$). This improved efficiency arises because, in the selective sparse case, the available coupling strength is directed primarily toward lasers with larger frequency detuning. Synchronization theory predicts that for nonidentical oscillators, the coupling must exceed the system's intrinsic frequency spread to achieve phase locking [1–3]. Concentrating coupling power on the most detuned lasers, as shown in Figs. S4(b–c), allows these elements to synchronize more rapidly and act as hubs that mediate global phase alignment across the entire array.

Figures S5(b) and S5(c) further illustrate the scalability of the selective sparse topology. We define a critical connectivity χ^* as the point where $\langle R \rangle = 0.9$, indicating strong synchronization of the dominant eigenmode. Repeating the analysis for arrays with $M = 50,\ 100, 200$ lasers reveals that χ^* decreases systematically with increasing M, following $\chi^* \propto 1/(M-1)$, consistent with the expected scaling behavior. Thus, larger arrays require fewer overall links to achieve global synchronization. However, if connectivity is reduced excessively in the selective sparse configuration, some lasers may become disconnected from the network. In practice, an optimal balance between selective and random coupling should therefore be employed for large-scale arrays.

Section A provides conceptual insight into the emergence of hub structures within the generalized time-delayed Kuramoto model. It demonstrates that the presence of a hub topology is a necessary, but not sufficient, condition for achieving synchronization in such systems. This finding clarifies why the simplified network of coupled linear oscillators yields consistent qualitative intuition regarding hub formation in the coupling matrix: near the steady-state, this linear model can be mapped onto the generalized Kuramoto framework. Within this architecture, reducing the number of coupling links can simultaneously ease experimental implementation and promote global synchronization, both in amplitude and phase, while requiring minimal total coupling strength. Consequently, a coupling matrix that strategically blends characteristics of the selective-sparse and random-sparse topologies represents a promising design strategy. These considerations underpin the main-text investigation of the Lang–Kobayashi model within the effective thermodynamic potential framework.

4. EFFECTIVE THERMODYNAMIC POTENTIAL FOR THE LASER NETWORK

Starting from the complex Lang–Kobayashi equations [Eqs. (1) and (2) in the main text], we express the electric field in polar form as $E_i(t) = r_i(t)e^{i\Omega_i(t)}$, where $r_i(t)$ and $\Omega_i(t)$ denote the amplitude and phase, respectively. To separate the radial and angular components, we multiply both sides of the complex electric-field equation by $e^{-i\Omega_i(t)}/r_i(t)$. The real and imaginary parts of the resulting expression then describe the amplitude and phase dynamics, respectively. The corresponding coupled Lang–Kobayashi equations in polar coordinates [4, 5] are given by

$$\begin{aligned}
\frac{\dot{r}_i(t)}{r_i(t)} &= \frac{1}{2}[G(N_i(t), r_i(t)) - \gamma] + \sum_{j=1}^{M} K_{ij}\frac{r_j(t-\tau)}{r_i(t)}\cos[\Omega_j(t-\tau) - \Omega_i(t) - \omega_0\tau], \\
\dot{\Omega}_i(t) &= \frac{\alpha}{2}[G(N_i(t), r_i(t)) - \gamma] + \Delta_i + \sum_{j=1}^{M} K_{ij}\frac{r_j(t-\tau)}{r_i(t)}\sin[\Omega_j(t-\tau) - \Omega_i(t) - \omega_0\tau], \\
\frac{\dot{N}_i(t)}{N_i(t)} &= \frac{J_0}{N_i(t)} - \gamma_n - \frac{G(N_i(t), r_i(t))r_i^2(t)}{N_i(t)},
\end{aligned} \tag{S3}$$

where the gain function is defined as

$$G(N_i(t), r_i(t)) = g\frac{N_i(t) - N_0}{1 + s\, r_i^2(t)}.$$

Next, we consider the optimal sparse network obtained using the island genetic algorithm. The corresponding steady-state solutions, shown in Figs. 2(b) and 2(c) of the main text, serve as the foundation for simplifying the Lang–Kobayashi equations:

$$r_i(t) \approx r_i^s, \;\; N_i(t) \approx N_i^s, \;\; \text{and} \;\; \frac{r_j(t-\tau)}{r_i(t)} \approx 1. \tag{S4}$$

Under these approximations, the Lang–Kobayashi equations reduce to:

$$0 = \frac{1}{2}[G(N_i^s, r_i^s) - \gamma] + \sum_{j=1}^{M} K_{ij}\cos[\Omega_j(t-\tau) - \Omega_i(t) - \omega_0\tau], \tag{S5}$$

$$\dot{\Omega}_i(t) = \frac{\alpha}{2}[G(N_i^s, r_i^s) - \gamma] + \Delta_i + \sum_{j=1}^{M} K_{ij}\sin[\Omega_j(t-\tau) - \Omega_i(t) - \omega_0\tau], \tag{S6}$$

$$0 = \frac{J_0}{N_i^s} - \gamma_n - \frac{G(N_i^s, r_i^s)(r_i^s)^2}{N_i^s}. \tag{S7}$$

By substituting the explicit form of the gain function from Eq. Eq. (**??**) into Eq. Eq. (**??**), the gain term in Eq. Eq. (**??**) is eliminated, yielding a phase equation that no longer explicitly depends on the gain. As a result, the phase dynamics depend only on the angular variables, effectively decoupling from both the amplitude and the carrier number. The resulting equation takes the form of a generalized time-delayed Kuramoto model[6] with an additional phase shift $\tan^{-1}\alpha + \omega_0\tau$:

$$\dot{\Omega}_i(t) = \Delta_i - \sqrt{1+\alpha^2}\sum_{j=1}^{M} K_{ij}\sin[\Omega_i(t) - \Omega_j(t-\tau) + \tan^{-1}\alpha + \omega_0\tau]. \tag{S8}$$

To derive the effective thermodynamic potential, we transform Eq. (S8) into the following gradient flow form:

$$\dot{\eta}_i(t) = -\frac{1}{\tau}\frac{d}{d\eta_i}U(\eta_i),$$

where the collective coupling influence of the other lasers on laser i is contained in the thermodynamic potential $U(\eta_i)$. The time-delayed phase difference is defined as

$$\eta_{ij}(t) = \Omega_i(t) - \Omega_j(t-\tau).$$

Associated with the steady-state synchronization solution, the phase variables $\Omega_i(t)$ and $\Omega_j(t)$ are proximal to each other. The second-order tensor $\eta_{ij}(t)$ of the phase differences can then be approximated by the following vector $\eta_i(t)$:

$$\eta_i(t) \approx \Omega_i(t) - \Omega_i(t-\tau). \tag{S9}$$

To proceed, we further assume a slow temporal evolution of the phase, so the finite difference can be approximated by the average derivative:

$$\frac{\eta_i(t)}{\tau} \approx \frac{\dot{\Omega}_i(t) + \dot{\Omega}_i(t-\tau)}{2}. \tag{S10}$$

Combining Eqs. (S9) and (S10), we get

$$\eta_i(t) \approx \tau\dot{\Omega}_i(t) - \frac{1}{2}\tau\dot{\eta}_i(t). \tag{S11}$$

Substituting this relation into the generalized time-delayed Kuramoto model [Eq. (S8)] and expanding about the synchronized steady-state solution, we obtain:

$$\dot{\eta}_i(t) = -\frac{1}{\tau}\left[2\eta_i(t) - 2\tau\Delta_i + 2\tau\sqrt{1+\alpha^2}\left(\sum_{j=1}^{M} K_{ij}\right)\sin[\eta_i(t) + \tan^{-1}\alpha + \omega_0\tau]\right]. \tag{S12}$$

The effective thermodynamic potential can then be identified as:

$$U(\eta_i(t)) = \eta_i^2(t) - 2\tau\Delta_i\eta_i(t) - 2\tau\sqrt{1+\alpha^2}k_i^{\text{in}}\cos[\eta_i(t) + \tan^{-1}\alpha + \omega_0\tau], \tag{S13}$$

and

$$k_i^{\text{in}} \equiv \sum_{j=1}^{M} K_{ij}$$

denotes the intrinsic coupling strength coming from other lasers to the ith laser. This expression generalizes the result for a single laser [7]:

$$U(\nu(t)) = \nu^2(t) - 2\tau\sqrt{1+\alpha^2}\gamma\cos[\nu(t) + \tan^{-1}\alpha + \omega_0\tau], \tag{S14}$$

where γ is the self-coupling strength and $\nu(t) \equiv \Omega(t) - \Omega(t-\tau)$. The thermodynamic potential in Eq. (S13) indicates that the effective coupling strength

$$\mathbb{K}_i \equiv \tau\sqrt{1+\alpha^2}k_i^{\text{in}}$$

is governed by the time delay τ, the linewidth enhancement factor α (responsible for amplitude–phase coupling), and the intrinsic coupling strength k_i^{in} (or γ for a single laser).

The local minima of the potential $U(\eta_i(t))$ can be determined through the first and second derivatives with respect to $\eta_i(t)$:

$$\frac{dU(\eta_i(t))}{d\eta_i(t)} = \eta_i(t) - \tau\Delta_i + \mathbb{K}_i\sin[\eta_i(t) + \tan^{-1}\alpha + \omega_0\tau] = 0, \tag{S15}$$

$$\frac{d^2U(\eta_i(t))}{d\eta_i^2(t)} = 1 + \mathbb{K}_i\cos[\eta_i(t) + \tan^{-1}\alpha + \omega_0\tau] > 0. \tag{S16}$$

Setting $\omega_0\tau \equiv 2k\pi$, Eqs. Eq. (S15) and Eq. (S16) can be further simplified as

$$\eta - \mathbb{F}_i = -\mathbb{K}_i\sin(\eta + \phi), \tag{S17}$$

$$1 + \mathbb{K}_i\cos(\eta + \phi) > 0, \tag{S18}$$

where $\mathbb{F}_i \equiv \tau\Delta_i$ denotes the effective detuning, and the constant phase shift is defined as

$$\phi \equiv \text{mod}(\tan^{-1}\alpha + \omega_0\tau, 2\pi) \approx 0.4\pi.$$

The variational principle dictates that the system's dynamical steady state converges to a local minimum of the potential. However, as the effective coupling strength increases, the number of possible steady-state solutions also grows. A nonzero amplitude–phase coupling factor, α, destabilizes these steady states [8–10], leading to the emergence of multiple basins of attraction. The cross intersections obtained from Eq. (**??**), highlighted by the red dots in Fig. 5 in the main text, represent the time-delayed phase difference

$$\eta_i^*(t) \approx \Omega_i^{fit}\tau + \varphi_i(t) - \varphi_i(t-\tau).$$

In the case of complete synchronization, the solutions of η_i become independent of the laser index i and reduce to

$$\eta^* \approx \Omega^{fit}\tau = 2\pi f_{\text{final}}\tau,$$

for $\varphi_i(t) \approx \varphi_i(t-\tau)$. To compensate for frequency disorders and ensure that η^* is independent of the laser index i, the effective coupling must be sufficiently strong: For an arbitrary laser i, the effective coupling strength should exceed the effective detuning, i.e., $\mathbb{K}_i > \mathbb{K}_i^c = |\mathbb{F}_i|$, or

$$k_i^{\text{in}} > |\Delta_i|/\sqrt{1+\alpha^2}.$$

Here, $\mathbb{K}_i^c$ represents the critical effective coupling strength required for laser i to sustain steady-state solutions. When the effective coupling exceeds this threshold, the solutions of η_i for all lasers can reside within the same regime, $1 + \mathbb{K}_i \cos(\eta + \phi) > 0$, corresponding to near-synchronized steady states. In this regime, the maximum final frequency difference is determined by the width of the allowed range. As the effective coupling continues to increase, the final frequency difference gradually decreases, while the presence of nonzero amplitude–phase coupling induces the formation of multiple attractors and ultimately triggers the onset of chaotic dynamics. A more detailed discussion of these behaviors is presented in the next section.

5. PHYSICAL UNDERSTANDING OF THE OPTIMAL SPARSE NETWORK STRUCTURE

A. Direct intuition for the hub structure

The complete frequency and phase synchronization in the steady state remains challenging for homogeneous all-to-all coupled networks, due to the non-negligible effects of frequency disorder. Starting from the generalized time-delayed Kuramoto model in Eq. (S8), a fully synchronized steady state requires identical frequency and phase evolution in the radial part, i.e., $\Omega_i(t) \approx \Omega_j(t) \approx \Omega_s t + \varphi_s(t)$. This leads to the relation

$$\Omega_i(t) - \Omega_j(t-\tau) = \Omega_s\tau + \varphi_s(t) - \varphi_s(t-\tau).$$

Substituting it into the phase dynamics in Eq. (S8) yields:

$$\begin{aligned}\Omega_s + \dot{\varphi}_s(t) = \Delta_i - \sqrt{1+\alpha^2}\sin\big[&\Omega_s\tau + \varphi_s(t) - \varphi_s(t-\tau) \\ &+ \tan^{-1}\alpha + \omega_0\tau\big]\sum_{j=1}^{M} K_{ij},\end{aligned} \tag{S19}$$

where the homogeneous all-to-all coupling implies the constant coupling strength per laser:

$$\sum_{j=1}^{M} K_{ij} = k_i^{\text{in}} = \kappa(M-1)$$

for all i. This uniformity limits the system's ability to satisfy the phase dynamics equation across all Δ_i, thereby precluding a fully synchronized solution when the effect of frequency disorder is non-negligible.

Can an optimal solution be found which supports complete frequency and phase synchronization for inhomogeneous networks? In this case, the quantity $\sum_{j=1}^{M} K_{ij}$ can vary with the laser index i, denoted as k_i^{in}. This leads to variations in the oscillation amplitude $\propto k_i^{\text{in}}$, which, if appropriately configured, can reduce the number of steady-state solutions and shrink the final frequency differences within the regime satisfying $1 + \mathbb{K}_i \cos(\eta + \phi) > 0$. However, if the variation is too large or deviates significantly from the optimal configuration, synchronization deteriorates—consistent with the results shown in Fig. S1.

Moreover, Eq. (S19) suggests that, to compensate for the effects of frequency disorder, the coupling strength per laser should be proportional to the frequency detuning, i.e., $k_i^{\text{in}} \propto c(t)\Delta_i$, where $c(t)$ is a general time-dependent coefficient arising from the time-dependent phase terms. This hub relationship is a necessary but not sufficient condition for the optimal sparse network. By significantly reducing the number of steady-state solutions and adaptively adjusting the effective coupling strength for each laser, these structures enable near-complete frequency and phase synchronization.

B. Sparse network analyzed via the thermodynamic potential theory

Based on the thermodynamic potential theory, a more quantitative understanding can be gained. In particular, for a sparse network with a binary sparse matrix in the presence of frequency disorder, the thermodynamic potential associated with each laser takes the form

$$U(\eta_i(t)) = \eta_i^2(t) - 2\tau\Delta_i\eta_i(t) - 2\tau\sqrt{1+\alpha^2}\kappa^f\xi_i\cos[\eta_i(t) + \tan^{-1}\alpha + \omega_0\tau]), \tag{S20}$$

where $k_i^{\text{in}} = \kappa^f\xi_i$ with $\kappa^f = 1\,\text{ns}^{-1}$ denoting the feedback coupling coefficient and ξ_i representing the number of connections for the ith laser due to the binary sparse nature of the network. To simplify, the effective coupling per laser is

$$\mathbb{K}_i \equiv \tau\sqrt{1+\alpha^2}\kappa^f\xi_i.$$

The total number of connections is given by

$$\sum_{i=1}^{M}\xi_i = \chi\, M(M-1). \tag{S21}$$

The underlying physical picture is that the island-based genetic algorithm constructs optimal sparse networks in which variations in ξ_i across different lasers compensate for the effects of frequency disorder. Beyond this tailored design for disorder compensation, the imposed sparsity also reduces the overall effective coupling strength, thereby mitigating multistability and promoting stable synchronized dynamics. Consequently, the networked laser system evolves toward a steady state characterized by both frequency and phase synchronization.

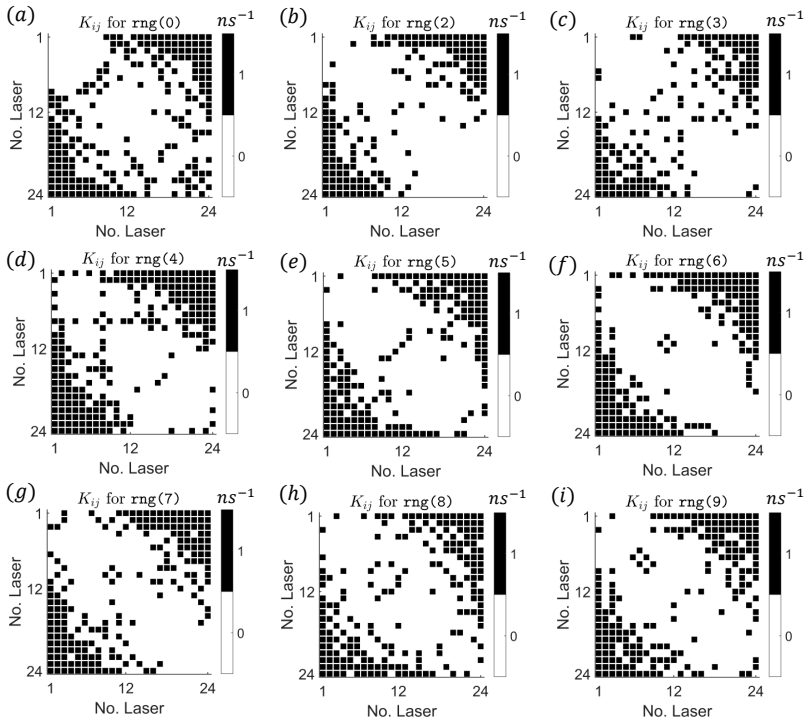

Fig. S6. Optimal sparse coupling matrices for nine different frequency-disorder realizations. (a-i) Binary color-encoded optimized coupling matrices corresponding to the frequency disorder $\Delta = 14 \times \mathcal{N}(0,1)$ rad/ns, generated using random seeds `rng(0)` to `rng(9)`, excluding `rng(1)`.

To compensate for frequency disorder in Eq. (S17) and Eq. (S18), the effective coupling strength for each laser must exceed its effective detuning, i.e., $\mathbb{K}_i > |\mathbb{F}_i| = \tau|\Delta_i|$. This condition imposes a lower bound on the number of connections ξ_i for the i-laser such that

$$\xi_i > |\Delta_i|/(\kappa^f\sqrt{1+\alpha^2})$$

ensuring the existence of steady-state solutions at small values and a narrow region of η. This criterion is consistent with the observed hub structure, where lasers with larger local detuning require a greater number of connections to maintain synchronization, as shown in Fig. S6. Figures S6(a–i) display the optimized sparse binary coupling matrices corresponding to different realizations of the frequency disorder. The row sum of each matrix, representing the number of connections of laser i, further supports the trends reported in the main text by illustrating how connectivity adapts to local detuning variations.

Accordingly, the extreme detuning sets the lower bound for the optimal number of connections ξ^* required to achieve synchronization across all lasers. Under the frequency disorder profile $\Delta_i = 14 \times \mathcal{N}(0,1)$ rad/ns with $M = 24$, the extreme detuning magnitude is approximately $|\Delta_0| \approx 30$ rad/ns, so

$$\xi^* > |\Delta_0|/(\kappa^f \sqrt{1+\alpha^2}).$$

Since the network connectivity parameter χ can be related to the number of connections by $\langle \xi_i \rangle = \chi(M-1)\,\mathrm{ns}^{-1}$ due to Eq. (S21), we get

$$\chi^* > \chi_c = |\Delta_0|/[\kappa^f (M-1)\sqrt{1+\alpha^2}] \approx 0.26. \tag{S22}$$

This estimate aligns with the simulation results in Fig. S2, where all synchronization peaks occur within the connectivity range of approximately 0.3 to 0.4. It also derives the scaling relation $\chi^* \propto 1/(M-1)$, consistent with the numerical results in Fig. 3 in the main text.

As illustrated in the schematic diagram in Fig. 5(a) of the main text, a uniform oscillation amplitude resulting from homogeneous all-to-all coupling does not guarantee consistency among all intersection points, η^*. This inconsistency indicates that the corresponding dynamic angular frequencies, $\Omega^{\mathrm{fit}} = \eta^*/\tau$, differ across lasers. Introducing sparsity into the network, by scaling the coupling strength with the number of connections, ξ_i, for each laser, helps fine-tune these intersections. As shown in Fig. 5(b) of the main text, variations in ξ_i adjust the values of η^*, bringing them into closer alignment. Furthermore, allowing an adaptive number of connections, ξ_i, substantially reduces the number of steady-state solutions and confines them to a narrower, lower-frequency domain compared with the homogeneous all-to-all coupling configuration.

6. ROBUSTNESS OF SYNCHRONIZATION IN SPARSE LASER NETWORKS

A. Robustness against dynamic and initial-state noises

Incorporating the dynamic and initial-condition noises into the Lang-Kobayashi equations leads to the following stochastic differential equations [4]:

$$\begin{aligned} dE_i(t)/dt = {} & \frac{1+i\alpha}{2}\left(g\frac{N_i(t)-N_0}{1+s|E_i(t)|^2} - \gamma\right)E_i(t) + i\Delta_i E_i(t) \\ & + e^{-i\omega_0\tau}\sum_{j=1}^{M} K_{ij}E_j(t-\tau) + F_{E_i}, \\ dN_i(t)/dt = {} & J_0 - \gamma_n N_i(t) - g\frac{N_i(t)-N_0}{1+s|E_i(t)|^2}|E_i(t)|^2 + F_{N_i}. \end{aligned} \tag{S23}$$

Depending on the wavelength, the natural frequency of the diode lasers lies on the order of 10^2 THz, which poses challenges for numerical simulation. It is conventional to adopt a rotating frame at the reference frequency $\omega_0 \equiv 2k\pi/\tau$ for some integer k so that the shift factor $\exp[-i\omega_0\tau]$ accounts for the phase accumulation induced by the time delay. Thus, the detuning of the i-th laser with true angular frequency ω_i is $\Delta_i = \omega_i - \omega_0$. The steady state of the uncoupled free-running lasers, $E_i^s(t) = r_s \exp[i\Delta_i t]$, where r_s is the steady-state electric field amplitude and $N_i(t) = N_s$, over the interval $t \in [-\tau, 0]$ can be set as the initial condition for fast convergence, where

$$\begin{aligned} r_s^2 &= [J_0 - \gamma_n(\gamma/g + N_0)]/[\gamma(1+\gamma_n s/g)], \\ N_s &= (1+sr_s^2)\gamma/g + N_0. \end{aligned}$$

A major source of dynamic noise in the diode lasers is spontaneous emission in the electric field given by [4]

$$\langle F_{E_i}(t), F_{E_j}^*(t')\rangle = R_{sp}\delta_{ij}\delta(t-t'), \tag{S24}$$

with R_{sp} being the spontaneous emission noise strength. This is essentially a Gaussian white noise. Another source of dynamic noise is the stochastic fluctuations in the carrier dynamics, which is multiplicative with intensity proportional to the carrier number:

$$\langle F_{N_i}(t), F_{N_j}(t')\rangle = \gamma_n N_i(t)\delta_{ij}\delta(t-t'). \tag{S25}$$

In addition to the noises due to spontaneous emission and carrier-number fluctuations, the initial conditions in the time-delay buffer are also subject to stochastic fluctuations, giving rise to another source of Gaussian noise in the complex electrical field and carrier number:

$$\Re[E_i^s(t)](1+\sigma_{\text{init}}\mathcal{N}(0,1)),\ \Im[E_i^s(t)](1+\sigma_{\text{init}}\mathcal{N}(0,1)),\ N_s(1+\sigma_{\text{init}}\mathcal{N}(0,1)). \tag{S26}$$

In our simulations, the Gaussian random variables in (S26) are independently generated for each laser and for each point in the initial time-delay interval. We integrate Eq. (S23) using MATLAB's `dde23` solver [11] in the noise-free case and employ the Adams–Bashforth–Moulton stochastic integration method [12] for the case with dynamic noise.

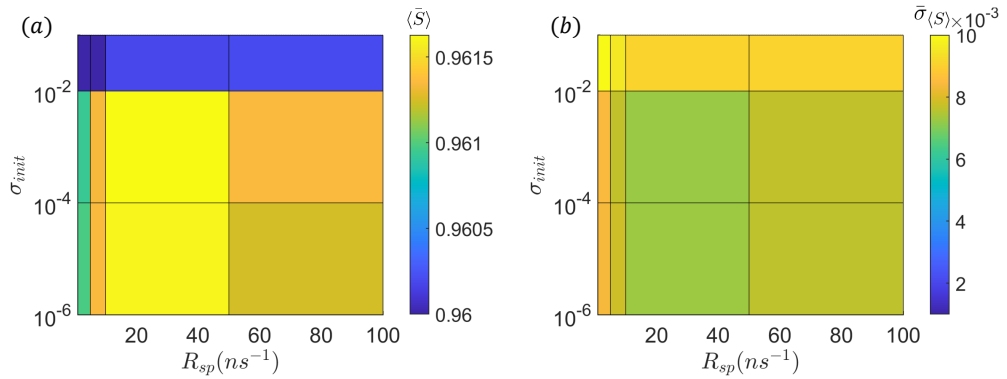

Fig. S7. Robust synchronization against dynamic and initial-condition noises. The optimal sparse laser network is from Fig. 2 in the main text, obtained from the island-based genetic algorithm. (a,b) Color-coded plot of the average synchronization strength $\langle\bar{S}\rangle$ and the standard deviation of $\langle S\rangle$, respectively, in the 2D parameter plane of $(R_{\text{sp}}, \sigma_{\text{init}})$, where four values are chosen for each parameter: $R_{\text{sp}} = \{5, 10, 50, 100\}$ ns^{-1} and $\sigma_{\text{init}} = \{10^{-6}, 10^{-4}, 10^{-2}, 10^{-1}\}$. For each combination of $\{\sigma_{\text{init}}, R_{\text{sp}}\}$, $\langle S\rangle$ is calculated using 100 independent realizations, which are used to calculate the the quantities $\langle\bar{S}\rangle$ and $\bar{\sigma}_{\langle S\rangle}$.

Our goal is to assess how robust the optimal sparse network in Figs. 2(b) and 2(c) of the main text is against the dynamic and initial-condition noises by calculating the average synchronization strength $\langle\bar{S}\rangle$ in the 2D parameter plane of $(R_{sp}, \sigma_{\text{init}})$. The results are shown in Figs. S7(a) and S7(b). Even under 10% initial-condition noise ($\sigma_{\text{init}} = 0.1$) and relatively large spontaneous emission noise ($R_{sp} = 100\, ns^{-1}$), stable and strong synchronization can be achieved, with fluctuations in the synchronization strength within about 0.2%. The results in Figs. S7(a) and S7(b) indicate that the optimal sparse networks found by the genetic algorithm can achieved robust synchronization against different types of noises in the diode lasers.

B. Robustness against random variations in frequency detuning, coupling strength, and pump rate

The optimal sparse network in Fig. 2(b) and 2(c) in the main text was obtained for a fixed set of frequency detuning disorders. What is the effect of random fluctuations in the frequency detuning on synchronization? To answer this question, we perturb the frequency disorder Δ_i to $\Delta_i + \sigma_\omega\mathcal{N}(0,1)$, where $\mathcal{N}(0,1)$ denotes a standard Gaussian random variable of zero mean and unit variance, as illustrated in Fig. S8(a). Remarkably, even when the perturbation strength σ_ω reaches approximately 35% of the original disorder strength σ_Δ, the synchronization strength $\langle S\rangle$ decreases only modestly: from 0.96 to 0.90 (a mere 6.7% reduction) as shown in Fig. S8(b). This result suggests that, insofar as the relative ordering of the frequency disorder magnitudes is preserved as shown in Fig. S8(a), strong frequency and phase synchronization associated with the optimal sparse network can be robustly maintained.

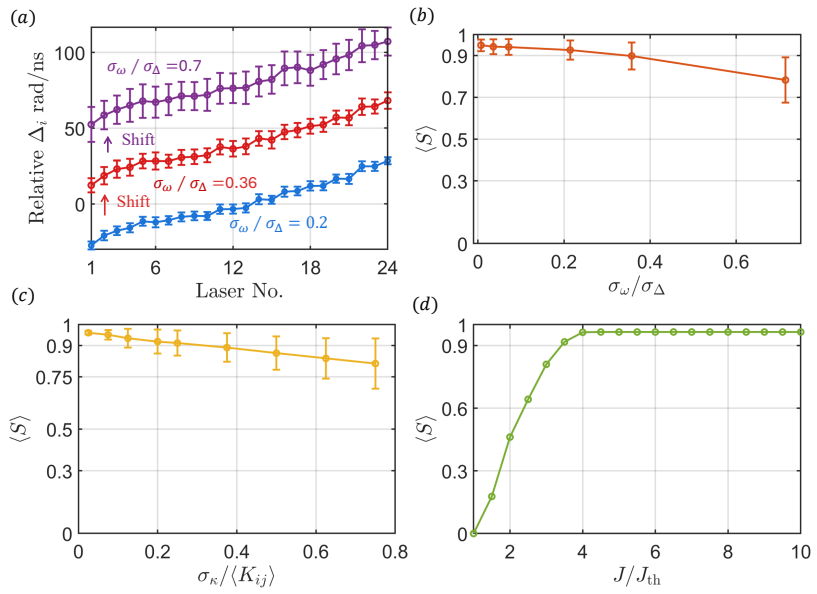

Fig. S8. Robustness in synchronization of the optimal sparse network against perturbations in frequency disorder, nodal coupling strength, and pump rate with the initial frequency standard deviation of $\sigma_\Delta = 14\,\mathrm{rad/ns}$. (a) Perturbation applied to the frequency detuning: $\Delta_i \to \Delta_i + \delta\omega_i$, where $\delta\omega_i = \sigma_\omega \mathcal{N}(0,1)$, with $\mathcal{N}(0,1)$ denoting a standard Gaussian random variable of zero mean and unit variance. Shown is the relative frequency detuning, shifted by 40 rad/ns, for $\sigma_\omega = 3$, 5 and 10 rad/ns, with standard error bars calculated from 100 random realizations. (b) Resulting synchronization strength as a function of σ_ω for $\sigma_\omega = 0.1, 0.5, 1, 3, 5, 10\,\mathrm{rad/ns}$, normalized by σ_Δ. Error bars denote the standard deviation over 100 random realizations at each σ_ω. (c) Synchronization strength $\langle S \rangle$ under perturbations to the nodal coupling strength: $K_{ij} \to K_{ij} + \delta K_{ij}$, where $\delta K_{ij} = \sigma_\kappa U(0,1)$, for $\sigma_\kappa = 0.01, 0.03, 0.05, 0.08, 0.1, 0.15, 0.2, 0.25, 0.3\,\mathrm{ns}^{-1}$. The mean coupling value is obtained by $\langle K_{ij} \rangle = \sum_{ij} K_{ij}/M^2 \approx \chi^*$. (d) Threshold pump rate $J_{\rm th} = \gamma_n(N_0 + \gamma/g)$. The pump is scanned over $J/J_{\rm th} \in [1, 10]$, and the corresponding synchronization measure $\langle S \rangle$ is plotted as a function of $J/J_{\rm th}$. In the present study, the operating pump is $J_0 = 4J_{\rm th} \approx 3.67 \times 10^8\,\mathrm{ns}^{-1}$.

What is the effect of random perturbations in the nodal coupling strengths of the optimal sparse network on synchronization? To answer this question, we introduce perturbations to the coupling matrix in the form $K_{ij} + \sigma_\kappa U(0,1)$, where $U(0,1)$ denotes a uniform random variable, as shown in Fig. S8(c), and the perturbations make the coupling configuration no longer binary. We find that the synchronization strength decreases approximately linearly as the perturbation strength σ_κ increases. The mean coupling is given by $\langle K_{ij} \rangle = \sum_{ij} K_{ij}/M^2 \approx \chi^*$ in the optimized sparse coupling network. As shown in Fig. S8(c), a 25% perturbation by $\sigma_\kappa/\langle K_{ij} \rangle$ leads to a comparable reduction in synchronization strength from 0.96 to 0.90 (a 6.7% reduction).

The pump rate also influences the degree of synchronization. When the pump rate is too low, the electric field is insufficiently excited, hindering synchronization. Conversely, when the pump rate is excessively high, the electric field saturates, offering no additional benefit to synchronization. In our analysis, the pump rate is evaluated in normalized form, $J/J_{\rm th} \in [1, 10]$. As the pump rate decreases from its original value [$J = 4J_{\rm th}$ in our study], synchronization tends to decline; however, a 13% reduction still yields a high synchronization level with $\langle S \rangle > 0.9$. In the opposite direction, increasing the pump rate beyond the original value leads to a saturation effect, with synchronization remaining nearly constant at higher pump levels.

Taken together, the results in Fig. S8 demonstrate the synchronization robustness of the optimal sparse network against perturbations in the frequency disorder, the nodal coupling strength and pump rate.

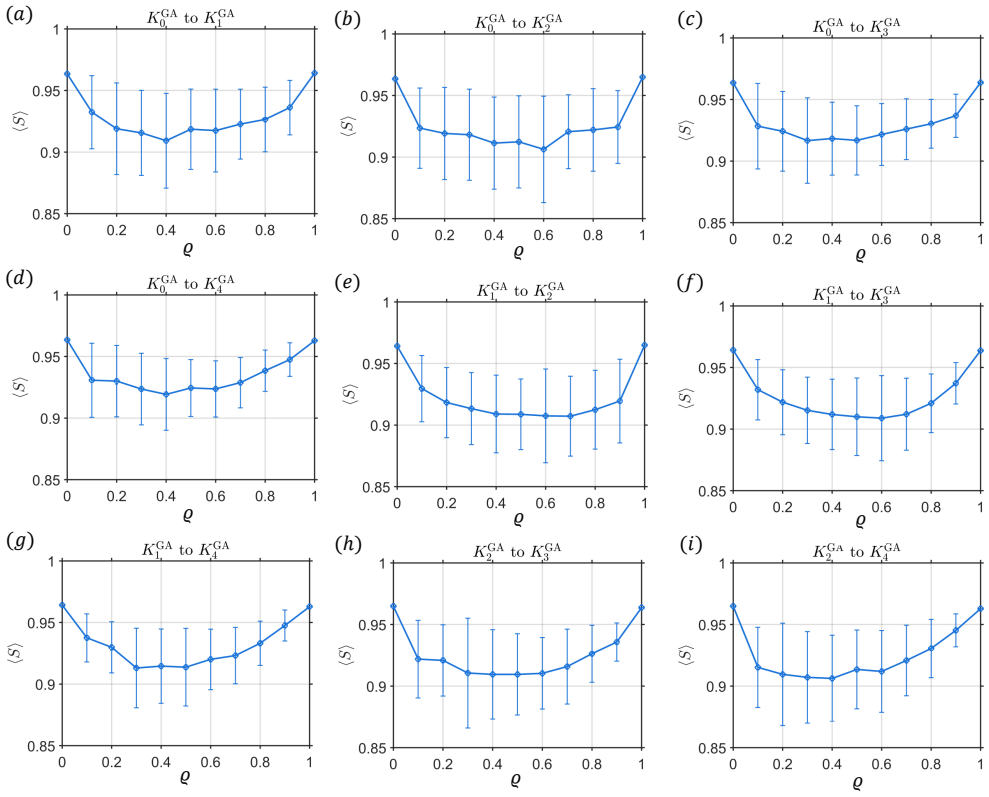

Fig. S9. Demonstration of the capability of island genetic algorithm in generating near optimal solutions of sparse network matrices. (a-i) Synchronization strength $\langle S \rangle$ for "mixed" optimal sparse networks. Five optimal networks are first generated by the genetic algorithm for $M = 24$ and $\Delta = 14 \times \mathcal{N}(0,1)$ rad/ns (from random seed `rng(1)`). The coupling matrices are interpolated (or "mixed") using the mixing parameter $\varrho \in [0,1]$ - see text for details. For each value of ϱ, 100 random realizations are used to calculate the average $\langle S \rangle$ value and its standard deviation. The fact that the $\langle S \rangle$ values in all cases remain high with relatively small variations implies that the genetic algorithm is capable of exploring diverse regions of the solution space to produce the optimal sparse network.

C. Optimization landscape for island genetic algorithm

In the main text, the random frequency disorder is generated according to $\Delta = 14 \times \mathcal{N}(0,1)$ rad/ns with the random seed `rng(1)` for a network of $M = 24$ lasers. Each independent run of the island genetic algorithm produces a distinct optimal sparse matrix that defines the network. Do these different optimal networks still possess a similar synchronization capability/behavior? As the optimal solutions correspond to some valley (peak) or minima (maxima) on the optimization landscape, equivalently one can ask whether the optimal networks (matrices) lie within the same basin of attraction [13]?

To address this question, we "mix" the optimal networks on a pairwise base and introduce a parameter $\varrho \in [0,1]$ to characterize the mixing. In particular, for a given frequency disorder configuration, five independent executions of the island-based genetic algorithm with identical hyperparameters but different random seeds yield five optimal coupling matrices, denoted as K_i^{GA} for $i = 0,1,2,3,4$. Since each matrix is required to be binary, a direct interpolation is not applicable. Instead, for any pair of matrices K_i^{GA} and K_j^{GA}, we define the difference matrix as $\Delta K_{ij}^{GA} = K_i^{GA} - K_j^{GA}$, whose zero elements correspond to the connections shared by the two matrices. To quantify the difference, we count the number of elements in the upper triangular part of ΔK_{ij}^{GA} with values equal to $-1\,ns^{-1}$ and $1\,ns^{-1}$, denoted as N_{ij}^{-1} and N_{ij}^{1}, respectively. Since all five optimal coupling matrices have the same connectivity level, the total coupling cost is identical across them, meaning that the total numbers of edges of the five matrices are the same,

implying $N_{ij}^{-1} = N_{ij}^{1}$. In fact, N_{ij}^{-1} is the number of links absent in K_i^{GA} but present in K_j^{GA}, i.e., $\{(m,n)|\Delta K_{ij}^{GA}(m,n) = -1\, ns^{-1}\}$, with N_{ij}^{1} corresponding to the links present in K_i^{GA} but absent in K_j^{GA}. In the mixing process, we retain all the common links (i.e., those with $\Delta K_{ij}^{GA} = 0$) but modify the rest by randomly selecting a fraction ϱ of the distinct links. Specifically, we randomly add ϱN_{ij}^{-1} links from the set in which K_j^{GA} has connections but K_i^{GA} does not, and remove ϱN_{ij}^{1} links from the set where K_i^{GA} has connections but K_j^{GA} does not. The resulting mixed matrix constructed from K_i^{GA} and K_j^{GA}, denoted as K_{mix}^{GA}, preserves the properties of being binary and symmetric with zero-diagonal constraints as described in the main text. By this construction, for $\varrho = 0$, we recover $K_{\text{mix}}^{GA} = K_i^{GA}$ and, for $\varrho = 1$, we have $K_{\text{mix}}^{GA} = K_j^{GA}$.

The optimization landscape revealed by this mixing process is illustrated in Figs. S9(a–i), where pairwise mixtures are performed among five independently optimal sparse coupling matrices. Each matrix differs from the others by approximately 30% of the links, yet all leading to similarly high synchronization performance, indicating that the genetic algorithm has effectively identified some local optimum with a relatively large basin of attraction. Note that, if the level of consistency in synchronization decreased, the mixed network configurations would reside in distinct valleys of a rugged, non-convex optimization landscape. Thus, even if there are multiple, well-separated basins of attraction, the genetic algorithm is capable of exploring diverse regions of the solution space to produce the optimal sparse network, in spite of the lack of guarantee that the algorithm would find the global optimum.

While the global optimum is unknown, the island genetic algorithm consistently discovers distinct, high-quality local optima in the sense of near-maximal synchronization, highlighting the algorithm's robustness and its ability to perform reliably in complex, non-convex combinatorial optimization problems. We find that, in the worst case of the mixing process, the synchronization measure remains about $\langle S \rangle = 0.9$, corresponding to only a 5% reduction from the best achievable value, further illustrating the robustness of the optimization landscape.

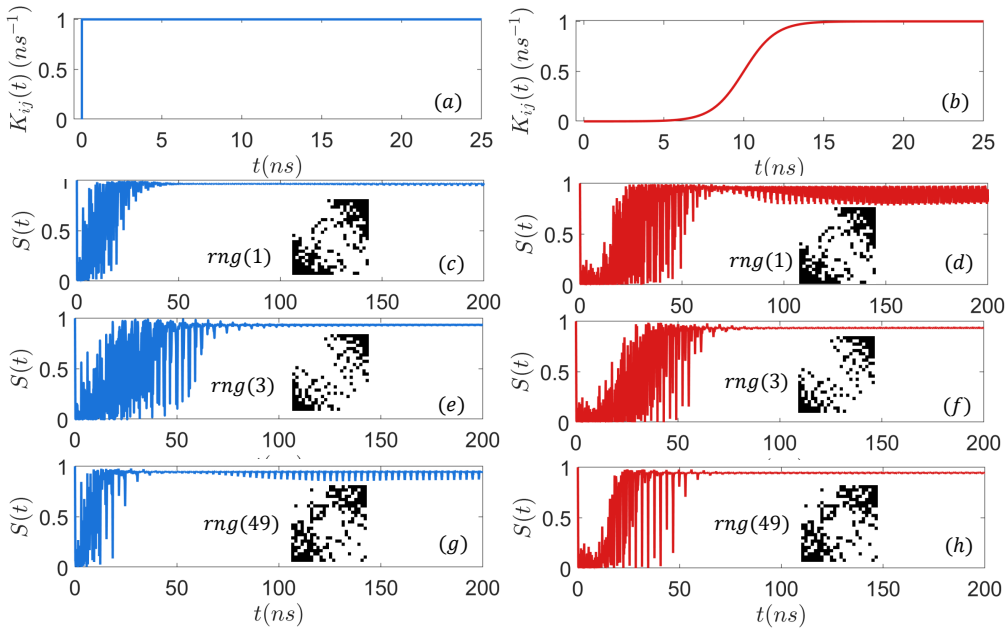

Fig. S10. Synchronization comparison between stepwise and smooth coupling ramps. Panels (a,b) illustrate two strategies for ramping the coupling strength, discontinuous (stepwise) and continuous via ($K_{ij}(t) = K_{ij}/[1 + \exp[-[t - 10]]]$), with the same target coupling configuration. Panels (c–h) report synchronization outcomes for three distinct frequency-disorder realizations (labeled by `rng`). Discontinuous ramps appear in (c,e,g), while continuous ramps appear in (d,f,h). In each pair (c,d), (e,f), and (g,h), the final coupling configuration after tens of nanoseconds is the same and fixed.

D. Synchronization under time-dependent coupling ramping

In our simulations so far, a discontinuous coupling profile over time is assumed, where the strength of each coupling element is turned on abruptly to a nonzero constant at $t = 0$, as shown in Fig. S10(a). Will a smooth, continuous coupling ramp, as shown in Fig. S10(b), affect synchronization? Figures S10(c–h) show, for $M = 24$, the time evolution of synchronization under several optimized sparse coupling configurations with a hub structure. These results indicate that, for a given coupling topology, different ramping schemes can have no significant effect on the final synchronization, in spite of small differences in the dynamical behavior of the synchronization measure. Overall, the choice of the way by which coupling is turned on has little effect on the final synchronization.

REFERENCES

1. N. Chopra and M. W. Spong, "On exponential synchronization of Kuramoto oscillators," IEEE Trans. Autom. Control. **54**, 353–357 (2009).
2. A. Jadbabaie, N. Motee, and M. Barahona, "On the stability of the Kuramoto model of coupled nonlinear oscillators," in *Proc. Amer. Control Conf. (ACC), 2004,* vol. 5 (IEEE, 2004), pp. 4296–4301.
3. F. Dörfler and F. Bullo, "On the critical coupling for kuramoto oscillators," SIAM J. Appl. Dyn. Syst. **10**, 1070–1099 (2011).
4. N. Nair, K. Hu, M. Berrill, *et al.*, "Using disorder to overcome disorder: A mechanism for frequency and phase synchronization of diode laser arrays," Phys. Rev. Lett. **127**, 173901 (2021).
5. R. Lang and K. Kobayashi, "External optical feedback effects on semiconductor injection laser properties," IEEE J. Quantum Electron. **16**, 347–355 (1980).
6. M. S. Yeung and S. H. Strogatz, "Time delay in the kuramoto model of coupled oscillators," Phys. Rev. Lett. **82**, 648 (1999).
7. D. Lenstra, "Statistical theory of the multistable external-feedback laser," Opt. Commun. **81**, 209–214 (1991).
8. H. G. Winful and S. S. Wang, "Stability of phase locking in coupled semiconductor laser arrays," Appl. Phys. Lett. **53**, 1894–1896 (1988).
9. H. G. Winful and L. Rahman, "Synchronized chaos and spatiotemporal chaos in arrays of coupled lasers," Phys. Rev. Lett. **65**, 1575 (1990).
10. L.-L. Ye, N. Vigne, F.-Y. Lin, *et al.*, "Disorder-mediated synchronization resonance in coupled semiconductor lasers," (2025).
11. L. F. Shampine and S. Thompson, "Solving ddes in matlab," Appl. Numer. Math. **37**, 441–458 (2001).
12. R. Toral and P. Colet, *Stochastic numerical methods: An introduction for students and scientists* (John Wiley & Sons, 2014).
13. F. Langhojer, D. Cardoza, M. Baertschy, and T. Weinacht, "Gaining mechanistic insight from closed loop learning control: The importance of basis in searching the phase space," J. Chem. Phys. **122** (2005).